Journal of Sound and Vibration 553 (2023) 117667

Contents lists available at ScienceDirect

Journal of Sound and Vibration

journal homepage: www.elsevier.com/locate/jsvi

A model of a rotating railway wheel for the prediction of sound radiation

V.T. Andrés [a], J. Martínez-Casas [a,*], F.D. Denia [a], D.J. Thompson [b]

[a] Instituto de Ingeniería Mecánica y Biomecánica, Universitat Politècnica de València, Camino de Vera s/n, 46022 Valencia, Spain
[b] Institute of Sound and Vibration Research, University of Southampton, Southampton SO17 1BJ, United Kingdom

ARTICLE INFO

Keywords:
Wheel vibroacoustic model
Railway wheelset
Rigid body motion
Rotation
Axisymmetry
Rolling noise

ABSTRACT

The axial symmetry of a railway wheel is taken into account to expand its vibrational response around the circumferential direction using Fourier series. This allows the vibroacoustic problem of the wheel to be formulated in a two-dimensional frame, solving for the dynamic and acoustic variables analytically in the circumferential direction. By adopting an Eulerian approach, the inertial effects associated with the rotation of the wheelset are included in the model, assuming a constant angular speed of rotation. To represent a railway wheelset, the wheel is constrained at the inner edge of the hub and the contribution of the rigid body motion of the wheelset is superimposed on its response. The latter is evaluated analytically under the assumption of small rigid body displacements. The computational efficiency of the proposed methodology is found to be three orders of magnitude greater than a full three-dimensional methodology, without compromising the accuracy. The results are compared in terms of acoustic radiation with the commercial package Ansys, showing similar sound power levels in almost all the frequency range apart from some differences at low frequencies due to the use of an acoustic model based on radiation ratios.

1. Introduction

Noise pollution from railways can cause discomfort and even risk to people's health. For this reason, in recent decades, the development of quieter railway components through different techniques has proliferated; among these, is the implementation of damper elements, such as the use of viscoelastic layers on the wheel [1] and dynamic absorbers on the wheel and rail [2,3], as well as the search for optimal designs of the wheel [4,5], the study of perforation schemes for the wheel [6] and the analysis of the influence of track design on the radiated noise [7]. Generally, in the preliminary design phase of such treatments, numerous simulations are required to reach the optimal configuration in terms of noise mitigation. In situations with multiple design variables, the number of simulations that can be carried out is limited by the computational cost associated with the vibroacoustic calculation. Consequently, it is convenient to have efficient vibroacoustic models of the railway components. The present study focuses on the wheelset.

To evaluate the sound radiation from the wheel, it is first necessary to determine the vibrational field on its surface. The wheel vibration occurs in response to the excitation forces at the wheel–rail contact; on straight track, the main reason for this excitation is the existence of surface roughness on the wheel and rail running surfaces. The response of the wheelset to these interaction forces can be determined numerically using the Finite Element Method (FEM) [8]. In running conditions, the wheelset is rotating about

* Corresponding author.
E-mail addresses: vicanrui@upv.es (V.T. Andrés), jomarc12@mcm.upv.es (J. Martínez-Casas), fdenia@mcm.upv.es (F.D. Denia), djt@isvr.soton.ac.uk (D.J. Thompson).

https://doi.org/10.1016/j.jsv.2023.117667
Received 14 May 2022; Received in revised form 1 March 2023; Accepted 7 March 2023
Available online 10 March 2023

its main axis, which changes the dynamics of this component compared with the stationary case. In Ref. [9], Thompson proposed to include the wheel rotation by means of a moving load problem, excluding the gyroscopic and inertial effects associated with the rotation. Other authors have proposed models based on Lagrangian coordinates to include the convective effects in flexible rotors. Geradin and Kill [10] developed the equations of motion (EoM) in both rotating and inertial frames by defining a reference system associated with local deformations and assuming small angles of rotation about the axis; in their work, the axial and flexural dynamic behaviour of the rotor was analysed, while the torsional one was neglected. Genta and Tonoli [11] developed a formulation that includes the axial, flexural and torsional dynamic behaviour of thin rotating discs. More recently, Sheng et al. [12] proposed a FE model of a rotating railway wheel using an axisymmetric approach, which includes the vertical vibration of the wheel axis by taking into account the momentum law; this was used to solve the response of the wheel to a vertical harmonic wheel–rail force and it was shown that the displacement of the wheel contact point, formulated in an inertial frame, is also harmonic at the same frequency as the interaction force. When the rotating body interacts with other non-rotating structures, models based on Eulerian coordinates present a clear advantage over those based on Lagrangian coordinates, since the location of the interaction usually has a constant spatial position with respect to the inertial reference system. Fayos et al. [13] proposed a model based on Eulerian coordinates applied to the railway wheelset to give an efficient solution to the interaction with the track; to do this, they developed the EoM of the rotating body initially in Lagrangian coordinates and, then, a conversion to Eulerian coordinates was carried out. Later, Martínez-Casas et al. [14] developed the EoM of the rotating 3D wheelset directly in Eulerian coordinates, in a cartesian reference system. With a view to reducing the computational cost associated with the resolution of the dynamic problem, Baeza et al. [15] performed an expansion of the response around the circumferential direction using Fourier series, after transforming the EoM from a cartesian to a cylindrical reference system.

Once the vibrational field of the wheel has been computed, it is possible to evaluate its sound radiation. The most precise way to do this is by solving the air pressure field through a Fluid Structure Interaction (FSI) approach. In the literature, however, acoustic models can be found based on the use of radiation ratios, which have a lower computational cost. These are based on post-processing the vibrational field of the wheel surface, as proposed in Ref. [16]. In this reference, the wheel is constrained at the inner edge of the hub and the modelling of the axle is omitted, which gives a good approximation for the contribution to the radiation of the vibration modes with 2 or more nodal diameters; it is worth noting that, according to Ref. [8], these are the most important for rolling noise generation. However, the vibroacoustic behaviour of the wheelset in the low frequency range is influenced by the axle motion. To include this, the contribution of the rigid body modes of the wheelset can be added to the constrained wheel vibration [17].

In this work, a model of a rotating railway wheel which takes advantage of its axial symmetry is proposed. The wheel flexibility is considered and the wheelset rigid body motion (RBM) is superimposed on the wheel vibration. To do this, an analytical model of a rigid rotating wheelset is developed. Both the flexible wheel and rigid wheelset models can be applied to other rotating systems as long as there is axial symmetry. Regarding the former, the axisymmetric approach with Eulerian coordinates proposed by Baeza et al. [15] is extended through the direct formulation of the EoM in a cylindrical reference system. Subsequently, the acoustic model of Thompson [16] is considered to evaluate the acoustic radiation of the wheel, taking advantage of the periodicity of the response to formulate the sound field also in a two-dimensional frame. The wheel is constrained at the inner edge of the hub and the contribution of the wheelset RBM is included through the RB model developed. The accuracy of the results is studied by a comparison with the solution of the FSI problem computed with the commercial FE software Ansys [18]. Likewise, the computational efficiency of the proposed methodology is evaluated by benchmarking against a full three-dimensional methodology.

Following this introduction, Section 2 presents the dynamic model of the rotating rigid wheelset. Then, the three-dimensional vibroacoustic model of the rotating wheel is presented in Section 3. In Section 4, the expansion of the wheel response around the circumferential direction is introduced and the EoM and sound radiation are obtained in a two-dimensional frame. Some results are presented in Section 5 and the main conclusions are summarized in Section 6.

2. Rigid body motion of the wheelset

This section describes the methodology used to determine the equations of the RBM including rotation at a constant speed Ω about its axis. There are six degrees of freedom associated with the RBM, three translations $\boldsymbol{\tau} = \begin{pmatrix}\tau_1 & \tau_2 & \tau_3\end{pmatrix}^{\mathrm{T}}$ parallel to the cartesian axes in Fig. 1 and three rotations $\boldsymbol{\psi} = \begin{pmatrix}\psi_1 & \psi_2 & \psi_3\end{pmatrix}^{\mathrm{T}}$ about them. Although the RBM is associated with the cartesian axes, the EoM are developed in a cylindrical reference frame with radial r, circumferential θ and axial z components. Considering only the RBM, the position $\mathbf{q}$ of any particle of the wheelset during the motion can be expressed as follows:

$$\mathbf{q} = \mathbf{u} + \mathbf{s}(\mathbf{u}, t), \tag{1}$$

where $\mathbf{u} = \begin{pmatrix}r & 0 & z\end{pmatrix}^{\mathrm{T}}$ is the spatial position, expressed in an inertial frame, corresponding to that particle without the motion and $\mathbf{s} = \begin{pmatrix}s_r & s_\theta & s_z\end{pmatrix}^{\mathrm{T}}$ contains the displacements of the particle in the position $\mathbf{u}$ at instant t due to the RBM in the radial, circumferential and axial directions, respectively. These displacements can be divided into the contribution of the translational $\mathbf{s}_\tau$ and rotational $\mathbf{s}_\psi$ motions, which yields the following vectorial sum:

$$\mathbf{s} = \mathbf{s}_\tau + \mathbf{s}_\psi. \tag{2}$$

On the one hand, the vector $\mathbf{s}_\tau$ is related to the translational motion $\boldsymbol{\tau}$ by means of the transformation matrix between the cartesian and cylindrical frame $\boldsymbol{\Theta}_\tau$, which, according to the definition of the coordinate θ in Fig. 1, is given by:

$$\mathbf{s}_\tau = \begin{bmatrix}\sin(\theta) & 0 & \cos(\theta)\\ \cos(\theta) & 0 & -\sin(\theta)\\ 0 & 1 & 0\end{bmatrix}\boldsymbol{\tau} = \boldsymbol{\Theta}_\tau\boldsymbol{\tau}. \tag{3}$$

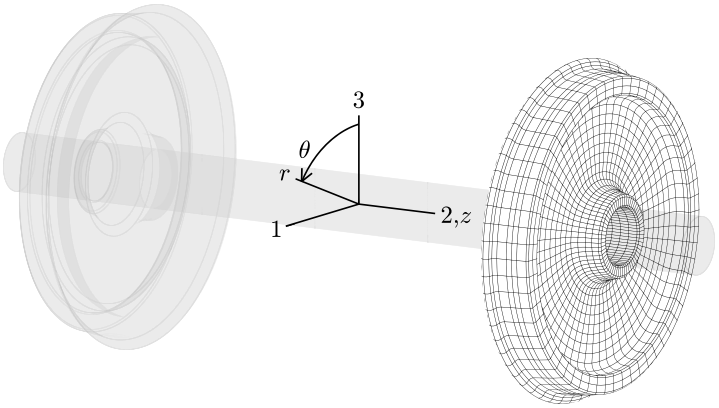

Fig. 1. Definition of the cartesian and cylindrical reference systems. The motion of the flexible wheel is evaluated through the FEM. The RBM of the wheelset, described analytically, is superimposed on it.

On the other hand, the vector $\mathbf{s}_\psi$ can be expressed as follows:

$$\mathbf{s}_\psi = \boldsymbol{\Theta}_\tau(\mathbf{R} - \mathbf{I}_{3\times3})\boldsymbol{\Theta}_\tau^{\mathrm{T}}\mathbf{u}, \tag{4}$$

where $\mathbf{I}_{3\times3}$ is the identity matrix of order 3×3 and the matrix $\mathbf{R}$ defines the position of a particle after the rigid body rotation expressed in an inertial frame and formulated in cartesian coordinates. Assuming small angles, this is given by:

$$\mathbf{R} = \begin{bmatrix} 1 & -\psi_3 & \psi_2 \\ \psi_3 & 1 & -\psi_1 \\ -\psi_2 & \psi_1 & 1 \end{bmatrix}. \tag{5}$$

After manipulating Eq. (4), the following relation between $\mathbf{s}_\psi$ and $\boldsymbol{\psi}$ is found:

$$\mathbf{s}_\psi = \begin{bmatrix} z\cos(\theta) & 0 & -z\sin(\theta) \\ -z\sin(\theta) & r & -z\cos(\theta) \\ -r\cos(\theta) & 0 & r\sin(\theta) \end{bmatrix} \boldsymbol{\psi} = \boldsymbol{\Theta}_\psi \boldsymbol{\psi}. \tag{6}$$

As the axis of rotation is coincident with the axial direction, i.e. $\boldsymbol{\Omega} = \begin{pmatrix} 0 & 0 & \Omega \end{pmatrix}^{\mathrm{T}}$ in the cylindrical frame, the velocity $\mathbf{v}_s$ due to the rigid body spinning is given by:

$$\mathbf{v}_s = \boldsymbol{\Omega} \times \mathbf{u} = r\Omega\hat{\mathbf{e}_2}, \tag{7}$$

with $\hat{\mathbf{e}_2} = \begin{pmatrix} 0 & 1 & 0 \end{pmatrix}^{\mathrm{T}}$. In an Eulerian approach, the velocity of any particle of the wheel can be evaluated as follows [19,20]:

$$\frac{\mathrm{D}\mathbf{q}}{\mathrm{D}t} = \mathbf{v}_s + \boldsymbol{\Theta}_\tau \dot{\boldsymbol{\tau}} + \boldsymbol{\Theta}_\psi \dot{\boldsymbol{\psi}} + \Omega \mathbf{Y} \boldsymbol{\psi}, \tag{8}$$

where the matrix $\mathbf{Y}$ is given by:

$$\mathbf{Y} = \begin{bmatrix} 0 & -r & 0 \\ 0 & 0 & 0 \\ r\sin(\theta) & 0 & r\cos(\theta) \end{bmatrix}. \tag{9}$$

The kinetic energy of the rotating wheelset due to its RBM is given by:

$$\begin{aligned} K =& \frac{1}{2}\int_{V_S} \rho \frac{\mathrm{D}\mathbf{q}^{\mathrm{T}}}{\mathrm{D}t}\frac{\mathrm{D}\mathbf{q}}{\mathrm{D}t}\mathrm{d}V = \\ =& \frac{1}{2}M\dot{\boldsymbol{\tau}}^{\mathrm{T}}\dot{\boldsymbol{\tau}} + \frac{1}{2}\dot{\boldsymbol{\psi}}^{\mathrm{T}}\boldsymbol{\mathcal{I}}\dot{\boldsymbol{\psi}} + \frac{1}{2}\Omega\mathcal{I}_z\dot{\boldsymbol{\psi}}^{\mathrm{T}}\mathbf{K}_1\boldsymbol{\psi} + \frac{1}{2}\Omega^2\mathcal{I}_z\boldsymbol{\psi}^{\mathrm{T}}\mathbf{K}_2\boldsymbol{\psi} + \Omega\mathcal{I}_z\dot{\boldsymbol{\psi}}^{\mathrm{T}}\hat{\mathbf{e}_2} + \frac{1}{2}\Omega^2\mathcal{I}_z, \end{aligned} \tag{10}$$

where ρ is the density of the material, V_S is the volume of the wheelset, M is its mass, $\mathcal{I}_z = \int_{V_S} \rho r^2 \mathrm{d}V$ is the moment of inertia about the axis of rotation, the matrices $\mathbf{K}_1$ and $\mathbf{K}_2$ are shown in Appendix A and $\boldsymbol{\mathcal{I}}$ is the inertia tensor of the wheelset that, given the cartesian reference system defined (see Fig. 1), can be expressed as:

$$\boldsymbol{\mathcal{I}} = \begin{bmatrix} \mathcal{I}_r & 0 & 0 \\ 0 & \mathcal{I}_z & 0 \\ 0 & 0 & \mathcal{I}_r \end{bmatrix}, \tag{11}$$

with $\mathcal{I}_r = \frac{I_z}{2} + \int_{V_S} \rho z^2 \mathrm{d}V$ being the moment of inertia about the radial axis. From the energy equation, Eq. (10), it follows that the translational and rotational motions are decoupled. The Lagrange equations for the translational motion are given by:

$$\frac{\mathrm{D}}{\mathrm{D}t}\left(\frac{\partial K}{\partial \dot{\boldsymbol{\tau}}}\right)^{\mathrm{T}} - \left(\frac{\partial K}{\partial \boldsymbol{\tau}}\right)^{\mathrm{T}} = M\ddot{\boldsymbol{\tau}}, \tag{12}$$

while for the rotation movement it is verified that:

$$\frac{\mathrm{D}}{\mathrm{D}t}\left(\frac{\partial K}{\partial \dot{\boldsymbol{\psi}}}\right)^{\mathrm{T}} - \left(\frac{\partial K}{\partial \boldsymbol{\psi}}\right)^{\mathrm{T}} = \boldsymbol{\mathcal{I}}\ddot{\boldsymbol{\psi}} + \Omega I_z \mathbf{K}_1 \dot{\boldsymbol{\psi}} - \Omega^2 I_z \mathbf{K}_2 \boldsymbol{\psi}. \tag{13}$$

In this work, it is considered that the external forces come from the wheel–rail interaction. Also, for simplicity, the contact is assumed to occur at the angular coordinate $\theta_c = 0$. Given the interaction forces $\mathbf{F} = \begin{pmatrix} F_r & F_\theta & F_z \end{pmatrix}^{\mathrm{T}}$ applied at the contact point, the six equations of the RBM are given by:

$$\begin{aligned} M\ddot{\boldsymbol{\tau}}(t) &= \begin{bmatrix} 0 & 1 & 0 \\ 0 & 0 & 1 \\ 1 & 0 & 0 \end{bmatrix} \mathbf{F}(t), \\ \boldsymbol{\mathcal{I}}\ddot{\boldsymbol{\psi}}(t) + \Omega I_z \mathbf{K}_1 \dot{\boldsymbol{\psi}}(t) - \Omega^2 I_z \mathbf{K}_2 \boldsymbol{\psi}(t) &= \begin{bmatrix} z_c & 0 & -r_c \\ 0 & r_c & 0 \\ 0 & -z_c & 0 \end{bmatrix} \mathbf{F}(t), \end{aligned} \tag{14}$$

where r_c and z_c are, respectively, the radial and axial coordinates of the contact point. For convenience, the EoM are transformed to the frequency domain. Considering a harmonic excitation of frequency ω and constant amplitude $\mathbf{F}(\omega)$, the steady state RBM is obtained by solving the following expressions:

$$\begin{aligned} -\omega^2 M \boldsymbol{\tau}(\omega) &= \begin{bmatrix} 0 & 1 & 0 \\ 0 & 0 & 1 \\ 1 & 0 & 0 \end{bmatrix} \mathbf{F}(\omega), \\ \begin{bmatrix} -\omega^2 \mathcal{I}_r - \frac{1}{2}\Omega^2 I_z & 0 & -\mathrm{i}\omega\Omega I_z \\ 0 & -\mathcal{I}_z(\omega^2 + \Omega^2) & 0 \\ \mathrm{i}\omega\Omega I_z & 0 & -\omega^2 \mathcal{I}_r - \frac{1}{2}\Omega^2 I_z \end{bmatrix} \boldsymbol{\psi}(\omega) &= \begin{bmatrix} z_c & 0 & -r_c \\ 0 & r_c & 0 \\ 0 & -z_c & 0 \end{bmatrix} \mathbf{F}(\omega), \end{aligned} \tag{15}$$

where i is the imaginary unit. The three translational motions and the rotation about the axial axis ψ_2 are decoupled from the other motions, while the rotations about the longitudinal ψ_1 and vertical ψ_3 axes are coupled to each other.

3. Three-dimensional vibroacoustic model of the wheel

In this section, the three-dimensional dynamic model developed by Martínez-Casas et al. [14] is formulated in a cylindrical reference system. This allows the axisymmetric approach to be developed in the next section. The models can be used to describe the dynamic behaviour of any rotating body with axial symmetry considering its flexibility and small RBM displacements. In this work, however, it is employed to evaluate the motion of a flexible railway wheel which is constrained at the inner edge of the hub and is rotating at a constant speed Ω about its main axis. After solving its vibroacoustic behaviour, the contribution of the RBM of the wheelset is included according to the developments of Section 2.

3.1. Kinetic energy

Given the rotating wheel subjected to an external dynamic force, the position $\mathbf{p}$ of any particle in the deformed shape can be expressed as the following vector sum:

$$\mathbf{p} = \mathbf{u} + \mathbf{w}(\mathbf{u}, t), \tag{16}$$

where $\mathbf{w} = \begin{pmatrix} w_r & w_\theta & w_z \end{pmatrix}^{\mathrm{T}}$ contains the displacements of the particle at the position $\mathbf{u}$ and instant t due to flexibility in the radial, circumferential and axial directions. The velocity of any particle of the wheel can be evaluated as follows [19,20]:

$$\frac{\mathrm{D}\mathbf{p}}{\mathrm{D}t} = \mathbf{v}_s + \dot{\mathbf{w}} + \Omega \frac{\partial \mathbf{w}}{\partial \theta} + \Omega \mathbf{J}\mathbf{w}, \tag{17}$$

where $\dot{\mathbf{w}} = \begin{pmatrix} \dot{w}_r & \dot{w}_\theta & \dot{w}_z \end{pmatrix}^{\mathrm{T}}$ contains the time derivatives of the displacements, $\frac{\partial \mathbf{w}}{\partial \theta} = \begin{pmatrix} \frac{\partial w_r}{\partial \theta} & \frac{\partial w_\theta}{\partial \theta} & \frac{\partial w_z}{\partial \theta} \end{pmatrix}^{\mathrm{T}}$ considers the derivatives with respect to the circumferential direction and the matrix $\mathbf{J}$ is specified in Appendix A. The kinetic energy E_k of the railway wheel

is given by:

$$\begin{aligned} E_k =& \frac{1}{2}\int_V \rho \frac{\mathrm{D}\mathbf{p}^{\mathrm{T}}}{\mathrm{D}t}\frac{\mathrm{D}\mathbf{p}}{\mathrm{D}t}\mathrm{d}V = \\ =& \frac{1}{2}\Omega^2\int_V \rho r^2 \mathrm{d}V + \frac{1}{2}\int_V \rho \dot{\mathbf{w}}^{\mathrm{T}}\dot{\mathbf{w}}\mathrm{d}V + \frac{1}{2}\Omega^2\int_V \rho \frac{\partial \mathbf{w}^{\mathrm{T}}}{\partial\theta}\frac{\partial \mathbf{w}}{\partial\theta}\mathrm{d}V + \Omega^2\int_V \rho \frac{\partial \mathbf{w}^{\mathrm{T}}}{\partial\theta}\mathbf{J}\mathbf{w}\mathrm{d}V + \\ &+\Omega\int_V \rho r\hat{\mathbf{e}}_2^{\mathrm{T}}\dot{\mathbf{w}}\mathrm{d}V + \Omega^2\int_V \rho r\hat{\mathbf{e}}_2^{\mathrm{T}}\frac{\partial \mathbf{w}}{\partial\theta}\mathrm{d}V + \Omega^2\int_V \rho r\hat{\mathbf{e}}_2^{\mathrm{T}}\mathbf{J}\mathbf{w}\mathrm{d}V + \\ &+\Omega\int_V \rho \dot{\mathbf{w}}^{\mathrm{T}}\frac{\partial \mathbf{w}}{\partial\theta}\mathrm{d}V + \Omega\int_V \rho \dot{\mathbf{w}}^{\mathrm{T}}\mathbf{J}\mathbf{w}\mathrm{d}V + \frac{1}{2}\Omega^2\int_V \rho \mathbf{w}^{\mathrm{T}}\mathbf{E}\mathbf{w}\mathrm{d}V, \end{aligned} \tag{18}$$

where V is the volume of the wheel, $\mathrm{d}V = r\mathrm{d}\theta\mathrm{d}r\mathrm{d}z$ and the matrix $\mathbf{E} = \mathbf{J}^{\mathrm{T}}\mathbf{J}$ can be found in Appendix A. Since the wheel is constrained at the inner edge of the hub, all the terms in the right hand side of Eq. (18) except the first one are associated with the wheel flexibility, while the first one is due to steady rolling.

3.2. Strain energy

The elastic potential energy E_p can be expressed as follows:

$$E_p = \frac{1}{2}\int_V \boldsymbol{\varepsilon}^{\mathrm{T}}\boldsymbol{\sigma}\mathrm{d}V = \frac{1}{2}\int_V \boldsymbol{\varepsilon}^{\mathrm{T}}\mathbf{D}\boldsymbol{\varepsilon}\mathrm{d}V, \tag{19}$$

where $\mathbf{D}$ is the material stiffness matrix obtained from Hooke's Law (see Appendix A). The strain vector satisfies $\boldsymbol{\varepsilon} = \mathbf{L}\mathbf{w} = \begin{pmatrix}\varepsilon_r & \varepsilon_\theta & \varepsilon_z & \gamma_{zr} & \gamma_{r\theta} & \gamma_{\theta z}\end{pmatrix}^{\mathrm{T}}$, with $\mathbf{L}$ being a matrix operator defined in Appendix A.

3.3. Virtual work

The roughness present on the wheel and rail running surfaces generates dynamic forces when the vehicle is travelling along the track. These forces are introduced in the wheel model as external loads applied at its contact point. The virtual work of the interaction forces $\mathbf{F} = \begin{pmatrix}F_r & F_\theta & F_z\end{pmatrix}^{\mathrm{T}}$ is given by:

$$\delta W = \delta\mathbf{w}^{\mathrm{T}}\mathbf{F}. \tag{20}$$

3.4. Equation of motion

A FE model is adopted, so that the displacement field in the eth element of the FE mesh is computed from the nodal solution by the following interpolation:

$$\mathbf{w}(r,\theta,z,t) = \mathbf{N}(r,\theta,z)\boldsymbol{w}^e(t), \tag{21}$$

$\mathbf{N}$ being the shape function matrix [21], which can be expressed as follows:

$$\mathbf{N} = \begin{bmatrix}\mathbf{N}_1 & \cdots & \mathbf{N}_j & \cdots & \mathbf{N}_m\end{bmatrix}; \qquad \mathbf{N}_j = N_j\begin{bmatrix}\cos(\theta-\theta_j) & \sin(\theta-\theta_j) & 0\\ -\sin(\theta-\theta_j) & \cos(\theta-\theta_j) & 0\\ 0 & 0 & 1\end{bmatrix}, \tag{22}$$

where subscript j refers to the jth node, m is the number of nodes in the eth element and N_j, which is dependent on the r, θ and z coordinates, is the shape function associated with the jth node. The vector $\boldsymbol{w}^e$ contains the displacements of the three Degrees of Freedom (DoF) of each node in the eth element, that is:

$$\boldsymbol{w}^e = \begin{pmatrix}\boldsymbol{w}_1^e & \cdots & \boldsymbol{w}_j^e & \cdots & \boldsymbol{w}_m^e\end{pmatrix}^{\mathrm{T}}; \qquad \boldsymbol{w}_j^e = \begin{pmatrix}w_{r,j}^e & w_{\theta,j}^e & w_{z,j}^e\end{pmatrix}. \tag{23}$$

By applying the expressions for the kinetic and strain energies in Eqs. (18) and (19) to the eth element and considering the FE approach of Eq. (21), the non-zero terms of the Lagrange equations are:

$$\frac{\mathrm{D}}{\mathrm{D}t}\left(\frac{\partial E_k}{\partial\dot{\boldsymbol{w}}^e}\right)^{\mathrm{T}} - \left(\frac{\partial E_k}{\partial\boldsymbol{w}^e}\right)^{\mathrm{T}} + \left(\frac{\partial E_p}{\partial\boldsymbol{w}^e}\right)^{\mathrm{T}} = \mathbf{M}^e\ddot{\boldsymbol{w}}^e + 2\Omega\mathbf{V}^e\dot{\boldsymbol{w}}^e + \left(\mathbf{K}^e + \Omega^2\mathbf{A}^e\right)\boldsymbol{w}^e - \Omega^2\mathbf{c}^e. \tag{24}$$

The element matrices in Eq. (24) correspond to the following expressions:

$$\begin{aligned} \mathbf{M}^e &= \int_{V^e}\rho\mathbf{N}^{\mathrm{T}}\mathbf{N}\mathrm{d}V,\\ \mathbf{V}^e &= \int_{V^e}\rho\mathbf{N}^{\mathrm{T}}\frac{\partial\mathbf{N}}{\partial\theta}\mathrm{d}V + \int_{V^e}\rho\mathbf{N}^{\mathrm{T}}\mathbf{J}\mathbf{N}\mathrm{d}V,\\ \mathbf{K}^e &= \int_{V^e}\mathbf{B}^{\mathrm{T}}\mathbf{D}\mathbf{B}\mathrm{d}V,\\ \mathbf{A}^e &= \int_{V^e}\rho\mathbf{N}^{\mathrm{T}}\frac{\partial^2\mathbf{N}}{\partial\theta^2}\mathrm{d}V + 2\int_{V^e}\rho\mathbf{N}^{\mathrm{T}}\mathbf{J}\frac{\partial\mathbf{N}}{\partial\theta}\mathrm{d}V - \int_{V^e}\rho\mathbf{N}^{\mathrm{T}}\mathbf{E}\mathbf{N}\mathrm{d}V,\\ \mathbf{c}^e &= \int_{V^e}\rho\mathbf{N}^{\mathrm{T}}\hat{\mathbf{e}}_1\mathrm{d}V, \end{aligned} \tag{25}$$

where V^e is the volume of the eth element, $\hat{\boldsymbol{\epsilon}}_1 = \begin{pmatrix}1 & 0 & 0\end{pmatrix}^{\mathrm{T}}$ and $\mathbf{B} = \mathbf{LN}$. As stated in [14], the second derivative in the matrix $\mathbf{A}^e$ can be reduced to a first derivative by integrating its first term by parts and therefore the convergence of the integral is guaranteed when C^0 shape functions are taken into account.

Following the FEM approach, the element matrices are assembled to obtain the global matrices of the equation of motion. The DoF (displacements of nodes) of the wheel are also assembled into the vector $\boldsymbol{w}$. Similarly, the interaction forces $\mathbf{F}$ applied on the wheel contact point are considered in the FE assembly of the forces (applied on all nodes and directions) into the vector $\mathcal{F}$. Thus, the EoM are given by:

$$\mathbf{M}\ddot{\boldsymbol{w}}(t) + 2\Omega\mathbf{V}\dot{\boldsymbol{w}}(t) + \left(\mathbf{K} + \Omega^2\mathbf{A}\right)\boldsymbol{w}(t) = \Omega^2\mathbf{c} + \mathcal{F}(t). \tag{26}$$

In order to evaluate the rolling noise radiated by the wheel, the model is transformed to the frequency domain, in which the EoM can be expressed for $\omega > 0$ as follows:

$$\left(-\omega^2\mathbf{M} + 2\mathrm{i}\omega\Omega\mathbf{V} + \mathbf{K} + \Omega^2\mathbf{A}\right)\boldsymbol{w}(\omega) = \mathcal{F}(\omega), \tag{27}$$

where $\boldsymbol{w}(\omega)$ represents the steady state response to a harmonic excitation of frequency ω and constant amplitude $\mathcal{F}(\omega)$.

3.5. Sound radiation

After solving the railway wheel dynamics, its acoustic radiation is computed by postprocessing the vibrational field on its surface. The radiation model employed in this work was developed by Thompson [16] and it establishes that the wheel sound power is obtained as the sum of the power associated with each set of modes with the same number of nodal diameters n. The wheel acoustic power W for a given frequency ω is evaluated as follows:

$$W(\omega) = \rho_f c \sum_{n\geq 0}\left(\sigma_{z,n}(\omega)S_z\langle\tilde{v}^2_{z,n}(\omega)\rangle + \sigma_{r,n}(\omega)S_r\langle\tilde{v}^2_{r,n}(\omega)\rangle\right), \tag{28}$$

where ρ_f is the density of air (fluid surrounding the wheel) and c is the speed of sound in air. The participation of each set of modes with n nodal diameters is in turn divided into its axial (subscript z) and radial (subscript r) contribution. Functions σ are the radiation ratios, which are numerically assessed in Ref. [16]. The wheel surface is projected normal to the axial and radial directions, which yields the areas S_z and S_r, respectively. Similarly, the squared velocity of the wheel surface is projected into the axial and radial directions and the corresponding values are averaged over time ($\tilde{\ }$) and space ($\langle\ \ \rangle$); these are given by:

$$\langle\tilde{v}^2_{i,n}\rangle = \frac{1}{2S_i}\int_S |v_{i,n}|^2 \mathrm{d}S_i, \quad i = z,r, \quad n \geq 0, \tag{29}$$

S being the wheel surface. In this work, the wheelset RBM is superimposed on the vibration of the wheel constrained at the inner edge of the hub. To do this, on the one hand, the EoM of the wheel given in Eq. (27) are solved and the vibrational velocity of any particle of the wheel $\dot{\mathbf{w}}(r,\theta,z,\omega)$ associated with its flexibility is obtained. On the other hand, the EoM of the rigid wheelset given in Eq. (15) are solved and the RB motions $\dot{\boldsymbol{\tau}}(\omega)$ and $\dot{\boldsymbol{\psi}}(\omega)$ are obtained; from these the vibrational velocity of any particle of the wheel $\dot{\mathbf{s}}(r,\theta,z,\omega)$ associated with the wheelset RBM can be found through the expressions in Eqs. (2), (3) and (6). Finally, both flexible and RB motions are superimposed. The wheelset RBM contributes to the response only for $n \leq 1$. Defining $\dot{w}|_n$ as the contribution to the velocity of the flexible wheel modes with n nodal diameters, then for $n = 0$ the total velocities of a wheel particle in the axial and radial directions are given by:

$$\begin{aligned} v_{z,0}(r,z,\omega) &= \dot{w}_z(r,z,\omega)|_{n=0} + \dot{\tau}_2(\omega), \\ v_{r,0}(r,z,\omega) &= \dot{w}_r(r,z,\omega)|_{n=0}, \end{aligned} \tag{30}$$

with $\dot{w}_z|_{n=0}$ and $\dot{w}_r|_{n=0}$ being associated with the wheel flexibility and $\dot{\tau}_2$ with the wheelset RBM. Likewise, the contribution of modes with $n = 1$ to the velocities is as follows:

$$\begin{aligned} v_{z,1}(r,\theta,z,\omega) &= \dot{w}_z(r,\theta,z,\omega)|_{n=1} - r\dot{\psi}_1(\omega)\cos(\theta) + r\dot{\psi}_3(\omega)\sin(\theta), \\ v_{r,1}(r,\theta,z,\omega) &= \dot{w}_r(r,\theta,z,\omega)|_{n=1} + (\dot{\tau}_3(\omega) + z\dot{\psi}_1(\omega))\cos(\theta) + (\dot{\tau}_1(\omega) - z\dot{\psi}_3(\omega))\sin(\theta), \end{aligned} \tag{31}$$

with $\dot{w}_z|_{n=1}$ and $\dot{w}_r|_{n=1}$ being associated with the wheel flexibility and the remaining terms with the wheelset RBM. Finally, for $n \geq 2$ the velocities are given by:

$$v_{i,n}(r,\theta,z,\omega) = \dot{w}_i(r,\theta,z,\omega)|_n, \quad i = z,r, \quad n \geq 2, \tag{32}$$

where there is no contribution from the wheelset RBM.

4. Vibroacoustic model: Axisymmetric approach

Given the axial symmetry of the wheel geometry, the displacement field can be expressed by means of an expansion as a Fourier series given by [22]:

$$\begin{aligned} w_r &= w_{r,0} + \sum_{n>0}\left(w_{r,n}\cos(n\theta) - \overline{w}_{r,n}\sin(n\theta)\right), \\ w_\theta &= -\overline{w}_{\theta,0} + \sum_{n>0}\left(w_{\theta,n}\sin(n\theta) - \overline{w}_{\theta,n}\cos(n\theta)\right), \\ w_z &= w_{z,0} + \sum_{n>0}\left(w_{z,n}\cos(n\theta) - \overline{w}_{z,n}\sin(n\theta)\right), \end{aligned} \tag{33}$$

n being an integer number representing each Fourier term, corresponding to the set of modes with n nodal diameters. In Eq. (33), the harmonic amplitudes without a bar represent symmetric motions about $\theta = 0$ and those with a bar represent antisymmetric motions about $\theta = 0$. It should be noted that the harmonic amplitudes $w_{r,0}$, $w_{z,0}$ and $\overline{w}_{\theta,0}$ (for $n = 0$) as well as $w_{r,n}$, $w_{\theta,n}$, $w_{z,n}$, $\overline{w}_{r,n}$, $\overline{w}_{\theta,n}$ and $\overline{w}_{z,n}$ (for $n > 0$) are dependent on the r, z and t coordinates but are independent of the θ coordinate.

4.1. Kinetic energy

Due to the harmonic description of the displacement field in the circumferential direction, the kinetic energy of the system described in Eq. (18) can be integrated analytically over this direction; details of the procedure are given in Appendix B. As a result, the kinetic energy can be divided into the contribution of each Fourier term and is therefore given by:

$$E_k = E_{k,0} + \sum_{n>0} E_{k,n}. \tag{34}$$

When considering a stationary body with axial symmetry, for each Fourier term the energy associated with the symmetric harmonic motion about $\theta = 0$ is also decoupled from the antisymmetric harmonic motion about $\theta = 0$. However, if the axisymmetric body is rotating, there is a coupling between these motions due to the 8th and 9th terms of the kinetic energy in the right hand side of Eq. (18). As a consequence, for each Fourier term both motions are simultaneously solved. The harmonic amplitudes in Eq. (33) are grouped for each Fourier term as follows:

$$\begin{aligned} \mathbf{w}_0 &= \begin{pmatrix} w_{r,0} & w_{z,0} & \overline{w}_{\theta,0} \end{pmatrix}^{\mathrm{T}}, && n = 0, \\ \mathbf{w}_n &= \begin{pmatrix} w_{r,n} & w_{\theta,n} & w_{z,n} & \overline{w}_{r,n} & \overline{w}_{\theta,n} & \overline{w}_{z,n} \end{pmatrix}^{\mathrm{T}}, && n > 0. \end{aligned} \tag{35}$$

The kinetic energy for $n = 0$ is given by:

$$\begin{aligned} E_{k,0} =& \pi\Omega^2 \int_A \rho r^3 \mathrm{d}A + \pi \int_A \rho r \dot{\mathbf{w}}_0^{\mathrm{T}} \dot{\mathbf{w}}_0 \mathrm{d}A - 2\pi\Omega \int_A \rho r^2 \hat{\mathbf{e}}_3^{\mathrm{T}} \dot{\mathbf{w}}_0 \mathrm{d}A + \\ &+ 2\pi\Omega^2 \int_A \rho r^2 \hat{\mathbf{e}}_1^{\mathrm{T}} \mathbf{w}_0 \mathrm{d}A + 2\pi\Omega \int_A \rho r \dot{\mathbf{w}}_0^{\mathrm{T}} \mathbf{J}_0 \mathbf{w}_0 \mathrm{d}A + \pi\Omega^2 \int_A \rho r \mathbf{w}_0^{\mathrm{T}} \mathbf{E}_0 \mathbf{w}_0 \mathrm{d}A, \end{aligned} \tag{36}$$

where A is the area of the wheel cross-section, $\mathrm{d}A = \mathrm{d}r\mathrm{d}z$, $\hat{\mathbf{e}}_3 = \begin{pmatrix} 0 & 0 & 1 \end{pmatrix}^{\mathrm{T}}$ and the matrices $\mathbf{J}_0$ and $\mathbf{E}_0$ are presented in Appendix A. The kinetic energy due to steady rolling, first term in the right hand side of Eq. (36), is not associated with vibration for $n = 0$ but is also included in the kinetic energy for $n = 0$, although it will not appear in the EoM. The kinetic energy $E_{k,n}$ for each $n > 0$ is expressed as follows:

$$\begin{aligned} E_{k,n} =& \frac{\pi}{2} \int_A \rho r \dot{\mathbf{w}}_n^{\mathrm{T}} \dot{\mathbf{w}}_n \mathrm{d}A + \frac{\pi}{2}\Omega^2 \int_A \rho r n^2 \mathbf{w}_n^{\mathrm{T}} \mathbf{w}_n \mathrm{d}A + 2\pi\Omega^2 \int_A \rho r n \mathbf{w}_n^{\mathrm{T}} \mathbf{J}_1 \mathbf{w}_n \mathrm{d}A + \\ &+ \pi\Omega \int_A \rho r n \dot{\mathbf{w}}_n^{\mathrm{T}} \mathbf{J}_2 \mathbf{w}_n \mathrm{d}A + \pi\Omega \int_A \rho r \dot{\mathbf{w}}_n^{\mathrm{T}} \mathbf{J}_3 \mathbf{w}_n \mathrm{d}A + \frac{\pi}{2}\Omega^2 \int_A \rho r \mathbf{w}_n^{\mathrm{T}} \mathbf{E}_3 \mathbf{w}_n \mathrm{d}A, \end{aligned} \tag{37}$$

with the matrices $\mathbf{J}_1$, $\mathbf{J}_2$, $\mathbf{J}_3$ and $\mathbf{E}_3$ being defined in Appendix A.

4.2. Strain energy

The strain energy in Eq. (19) can be integrated analytically over the circumferential direction according to the expansion of Eq. (33). Details of this are given in Appendix B. Similarly to the kinetic energy, the strain energy can be expressed as a sum of the contributions of each Fourier term, yielding the following expression:

$$E_p = E_{p,0} + \sum_{n>0} E_{p,n}. \tag{38}$$

Unlike the kinetic energy, for each Fourier term the contribution in the strain energy of the symmetric motion about $\theta = 0$ is decoupled from the antisymmetric motion about $\theta = 0$. Nevertheless, since the kinetic energy equation couples both motions, they are also considered simultaneously in the strain energy equation.

The strain energy $E_{p,0}$ for $n = 0$ is given by:

$$E_{p,0} = \pi \int_A r \boldsymbol{\varepsilon}_0^{\mathrm{T}} \mathbf{D} \boldsymbol{\varepsilon}_0 \mathrm{d}A, \tag{39}$$

where $\boldsymbol{\varepsilon}_0$ is defined as follows:

$$\boldsymbol{\varepsilon}_0 = \mathbf{L}_0 \mathbf{w}_0, \tag{40}$$

with $\mathbf{L}_0$ being a matrix derivative operator specified in Appendix A. The strain energy $E_{p,n}$ for $n > 0$ is given by:

$$E_{p,n} = \frac{\pi}{2} \int_A r \boldsymbol{\varepsilon}_n^{\mathrm{T}} \mathbf{D} \boldsymbol{\varepsilon}_n \mathrm{d}A + \frac{\pi}{2} \int_A r \bar{\boldsymbol{\varepsilon}}_n^{\mathrm{T}} \mathbf{D} \bar{\boldsymbol{\varepsilon}}_n \mathrm{d}A, \tag{41}$$

where $\boldsymbol{\epsilon}_n$ and $\overline{\boldsymbol{\epsilon}}_n$ are defined as follows:

$$\begin{aligned}\boldsymbol{\epsilon}_n &= (\mathbf{L}_a + n\mathbf{L}_b)\mathbf{w}_n,\\ \overline{\boldsymbol{\epsilon}}_n &= (\overline{\mathbf{L}}_a + n\overline{\mathbf{L}}_b)\mathbf{w}_n.\end{aligned} \tag{42}$$

The matrix operators $\mathbf{L}_a$, $\mathbf{L}_b$, $\overline{\mathbf{L}}_a$ and $\overline{\mathbf{L}}_b$ are specified in Appendix A.

4.3. Virtual work

Although the interaction forces $\mathbf{F}$ are modelled as point loads at the wheel contact, they can be expressed as a function of the circumferential coordinate θ. Therefore, they are defined in terms of the external force distribution $\mathbf{f}$, which is equivalent to $\mathbf{F}$, applied along the locus of points with the same radial and axial coordinates as the contact point. This can be written as:

$$\mathbf{f}(\theta) = \mathbf{F}\frac{\delta(\theta-\theta_c)}{r_c}, \tag{43}$$

with $\delta(\theta-\theta_c)$ being the Dirac delta function. The force distribution $\mathbf{f} = \begin{pmatrix} f_r & f_\theta & f_z \end{pmatrix}^{\mathrm{T}}$ can also be decomposed as a Fourier series with respect to the circumferential direction, which yields the following expressions:

$$\begin{aligned} f_r &= f_{r,0} + \sum_{n>0}\left(f_{r,n}\cos(n\theta) - \overline{f}_{r,n}\sin(n\theta)\right),\\ f_\theta &= -\overline{f}_{\theta,0} + \sum_{n>0}\left(f_{\theta,n}\sin(n\theta) - \overline{f}_{\theta,n}\cos(n\theta)\right),\\ f_z &= f_{z,0} + \sum_{n>0}\left(f_{z,n}\cos(n\theta) - \overline{f}_{z,n}\sin(n\theta)\right),\end{aligned} \tag{44}$$

where the harmonic force coefficients $f_{r,0}$, $f_{z,0}$, $\overline{f}_{\theta,0}$, $f_{r,n}$, $f_{\theta,n}$, $f_{z,n}$, $\overline{f}_{r,n}$, $\overline{f}_{\theta,n}$ and $\overline{f}_{z,n}$ are independent of θ and, considering the expression in Eq. (43), can be evaluated as follows:

$$\begin{aligned}
\begin{pmatrix} f_{r,0}\\ \overline{f}_{\theta,0}\\ f_{z,0}\end{pmatrix} &= \frac{1}{2\pi}\int_{-\pi}^{\pi}\begin{pmatrix} f_r\\ -f_\theta\\ f_z\end{pmatrix}\mathrm{d}\theta = \frac{1}{2\pi r_c}\begin{pmatrix} F_r\\ -F_\theta\\ F_z\end{pmatrix}, && n=0,\\
\begin{pmatrix} f_{r,n}\\ \overline{f}_{\theta,n}\\ f_{z,n}\end{pmatrix} &= \frac{1}{\pi}\int_{-\pi}^{\pi}\begin{pmatrix} f_r\\ -f_\theta\\ f_z\end{pmatrix}\cos(n\theta)\mathrm{d}\theta = \frac{1}{\pi r_c}\begin{pmatrix} F_r\\ -F_\theta\\ F_z\end{pmatrix}, && n>0,\\
\begin{pmatrix} \overline{f}_{r,n}\\ f_{\theta,n}\\ \overline{f}_{z,n}\end{pmatrix} &= \frac{1}{\pi}\int_{-\pi}^{\pi}\begin{pmatrix} -f_r\\ f_\theta\\ -f_z\end{pmatrix}\sin(n\theta)\mathrm{d}\theta = \begin{pmatrix} 0\\ 0\\ 0\end{pmatrix}, && n>0.
\end{aligned} \tag{45}$$

As in Section 2, it is assumed for simplicity that $\theta_c = 0$. The virtual work of the load $\mathbf{f}$ is given by:

$$\delta W = \int_{-\pi}^{\pi}\delta\mathbf{w}^{\mathrm{T}}\mathbf{f}r_c\mathrm{d}\theta. \tag{46}$$

Introducing the expansion of Eqs. (33) and (44) in Eq. (46) along with the relations in Eq. (45), the virtual work can also be decomposed into the contribution associated with each Fourier term as follows:

$$\delta W = \delta W_0 + \sum_{n>0}\delta W_n. \tag{47}$$

The virtual work for $n \geq 0$ is given by:

$$\delta W_n = \delta\mathbf{w}_n^{\mathrm{T}}\mathbf{F}_n, \quad n \geq 0, \tag{48}$$

where the force vector is defined as follows:

$$\begin{aligned}\mathbf{F}_0 &= \begin{pmatrix} F_r & F_z & -F_\theta\end{pmatrix}^{\mathrm{T}}, && n=0,\\ \mathbf{F}_n &= \begin{pmatrix} F_r & 0 & F_z & 0 & -F_\theta & 0\end{pmatrix}^{\mathrm{T}}, && n>0.\end{aligned} \tag{49}$$

4.4. Equation of motion

The harmonic amplitudes in Eq. (35) are the unknown DoF to be determined. Considering a FE model of the wheel cross-section, the following interpolation is proposed in the eth element for $n = 0$:

$$\mathbf{w}_0(r,z,t) = \mathbf{N}_0(r,z)\boldsymbol{w}_0^e(t), \tag{50}$$

where $\mathbf{N}_0$ is the shape function matrix defined for $n = 0$. When p nodes are considered in the wheel cross-section, this matrix is given by:

$$\mathbf{N}_0 = \begin{bmatrix}\mathbf{N}_{1,n=0} & \cdots & \mathbf{N}_{j,n=0} & \cdots & \mathbf{N}_{p,n=0}\end{bmatrix}; \qquad \mathbf{N}_{j,n=0} = N_j\mathbf{I}_{3\times 3}, \tag{51}$$

The vector of harmonic amplitudes of the eth element $\boldsymbol{w}_0^e$ can be expressed as follows:

$$\boldsymbol{w}_0^e = \begin{pmatrix} \boldsymbol{w}_{1,n=0}^e & \cdots & \boldsymbol{w}_{j,n=0}^e & \cdots & \boldsymbol{w}_{p,n=0}^e \end{pmatrix}^{\mathrm{T}}; \qquad \boldsymbol{w}_{j,n=0}^e = \begin{pmatrix} w_{r,j,n=0}^e & w_{z,j,n=0}^e & \overline{w}_{\theta,j,n=0}^e \end{pmatrix}. \tag{52}$$

Similar to the three-dimensional model, the Lagrange equations for motion with $n = 0$ are given by:

$$\frac{\mathrm{D}}{\mathrm{D}t}\left(\frac{\partial E_{k,0}}{\partial \dot{\boldsymbol{w}}_0^e}\right)^{\mathrm{T}} - \left(\frac{\partial E_{k,0}}{\partial \boldsymbol{w}_0^e}\right)^{\mathrm{T}} + \left(\frac{\partial E_{p,0}}{\partial \boldsymbol{w}_0^e}\right)^{\mathrm{T}} = \mathbf{M}_0^e \ddot{\boldsymbol{w}}_0^e + 2\Omega \mathbf{V}_0^e \dot{\boldsymbol{w}}_0^e + \left(\mathbf{K}_0^e + \Omega^2 \mathbf{A}_0^e\right) \boldsymbol{w}_0^e - \Omega^2 \mathbf{c}_0^e, \tag{53}$$

from which the following element matrices are defined:

$$\begin{aligned} \mathbf{M}_0^e &= 2\pi \int_{A^e} \rho r \mathbf{N}_0^{\mathrm{T}} \mathbf{N}_0 \mathrm{d}A, \\ \mathbf{V}_0^e &= 2\pi \int_{A^e} \rho r \mathbf{N}_0^{\mathrm{T}} \mathbf{J}_0 \mathbf{N}_0 \mathrm{d}A, \\ \mathbf{K}_0^e &= 2\pi \int_{A^e} r \mathbf{B}_0^{\mathrm{T}} \mathbf{D} \mathbf{B}_0 \mathrm{d}A, \\ \mathbf{A}_0^e &= -2\pi \int_{A^e} \rho r \mathbf{N}_0^{\mathrm{T}} \mathbf{E}_0 \mathbf{N}_0 \mathrm{d}A, \\ \mathbf{c}_0^e &= 2\pi \int_{A^e} \rho r^2 \mathbf{N}_0^{\mathrm{T}} \widehat{\mathbf{e}}_1 \mathrm{d}A, \end{aligned} \tag{54}$$

where A^e is the area of the eth element and $\mathbf{B}_0 = \mathbf{L}_0 \mathbf{N}_0$. These element matrices can be assembled to obtain the global matrices of the EoM for $n = 0$. In the same way, the displacement DoF are assembled into the vector $\boldsymbol{w}_0$ and the forces applied at the contact point and defined by $\mathbf{F}_0$ in Eq. (49) are assembled into the vector $\boldsymbol{\mathcal{F}}_0$. Finally, the EoM are given by:

$$\mathbf{M}_0 \ddot{\boldsymbol{w}}_0(t) + 2\Omega \mathbf{V}_0 \dot{\boldsymbol{w}}_0(t) + \left(\mathbf{K}_0 + \Omega^2 \mathbf{A}_0\right) \boldsymbol{w}_0(t) = \Omega^2 \mathbf{c}_0 + \boldsymbol{\mathcal{F}}_0(t). \tag{55}$$

As in the 3D approach, the model can be transformed to the frequency domain, in which the EoM are given for $\omega > 0$ by:

$$\left(-\omega^2 \mathbf{M}_0 + 2\mathrm{i}\omega\Omega \mathbf{V}_0 + \mathbf{K}_0 + \Omega^2 \mathbf{A}_0\right) \boldsymbol{w}_0(\omega) = \boldsymbol{\mathcal{F}}_0(\omega). \tag{56}$$

The same procedure is carried out for each $n > 0$. In this case, the harmonic amplitudes in the eth element are interpolated by:

$$\mathbf{w}_n(r, z, t) = \mathbf{N}_\eta(r, z) \boldsymbol{w}_n^e(t), \tag{57}$$

where the shape function matrix for $n > 0$ $\mathbf{N}_\eta$ is independent of n and is defined as follows:

$$\mathbf{N}_\eta = \begin{bmatrix} \mathbf{N}_{1,\eta} & \cdots & \mathbf{N}_{j,\eta} & \cdots & \mathbf{N}_{p,\eta} \end{bmatrix}; \qquad \mathbf{N}_{j,\eta} = N_j \mathbf{I}_{6\times 6}, \tag{58}$$

with $\mathbf{I}_{6\times 6}$ being the identity matrix of order 6×6. The harmonic amplitude vector in the eth element is given by:

$$\boldsymbol{w}_n^e = \begin{pmatrix} \boldsymbol{w}_{1,n}^e & \cdots & \boldsymbol{w}_{j,n}^e & \cdots & \boldsymbol{w}_{p,n}^e \end{pmatrix}^{\mathrm{T}}; \qquad \boldsymbol{w}_{j,n}^e = \begin{pmatrix} w_{r,j,n}^e & w_{\theta,j,n}^e & w_{z,j,n}^e & \overline{w}_{r,j,n}^e & \overline{w}_{\theta,j,n}^e & \overline{w}_{z,j,n}^e \end{pmatrix}. \tag{59}$$

Thus, the Lagrange equations for each n greater than zero can be expressed as the following matrix system:

$$\frac{\mathrm{D}}{\mathrm{D}t}\left(\frac{\partial E_{k,n}}{\partial \dot{\boldsymbol{w}}_n^e}\right)^{\mathrm{T}} - \left(\frac{\partial E_{k,n}}{\partial \boldsymbol{w}_n^e}\right)^{\mathrm{T}} + \left(\frac{\partial E_{p,n}}{\partial \boldsymbol{w}_n^e}\right)^{\mathrm{T}} = \mathbf{M}_\eta^e \ddot{\boldsymbol{w}}_n^e + 2\Omega \mathbf{V}_n^e \dot{\boldsymbol{w}}_n^e + \left(\mathbf{K}_n^e + \Omega^2 \mathbf{A}_n^e\right) \boldsymbol{w}_n^e, \tag{60}$$

the element matrices being as follows:

$$\begin{aligned} \mathbf{M}_\eta^e &= \pi \int_{A^e} \rho r \mathbf{N}_\eta^{\mathrm{T}} \mathbf{N}_\eta \mathrm{d}A, \\ \mathbf{V}_n^e &= \pi \int_{A^e} \rho r \mathbf{N}_\eta^{\mathrm{T}} \mathbf{J}_3 \mathbf{N}_\eta \mathrm{d}A + n\pi \int_{A^e} \rho r \mathbf{N}_\eta^{\mathrm{T}} \mathbf{J}_2 \mathbf{N}_\eta \mathrm{d}A, \\ \mathbf{K}_n^e &= \pi \int_{A^e} r \left(\mathbf{B}_a^{\mathrm{T}} + n\mathbf{B}_b^{\mathrm{T}}\right) \mathbf{D} \left(\mathbf{B}_a + n\mathbf{B}_b\right) \mathrm{d}A + \pi \int_{A^e} r \left(\overline{\mathbf{B}}_a^{\mathrm{T}} + n\overline{\mathbf{B}}_b^{\mathrm{T}}\right) \mathbf{D} \left(\overline{\mathbf{B}}_a + n\overline{\mathbf{B}}_b\right) \mathrm{d}A, \\ \mathbf{A}_n^e &= -\pi \int_{A^e} \rho r \mathbf{N}_\eta^{\mathrm{T}} \mathbf{E}_3 \mathbf{N}_\eta \mathrm{d}A - n2\pi \int_{A^e} \rho r \mathbf{N}_\eta^{\mathrm{T}} (\mathbf{J}_1^{\mathrm{T}} + \mathbf{J}_1) \mathbf{N}_\eta \mathrm{d}A - n^2 \pi \int_{A^e} \rho r \mathbf{N}_\eta^{\mathrm{T}} \mathbf{N}_\eta \mathrm{d}A, \end{aligned} \tag{61}$$

where $\mathbf{B}_a = \mathbf{L}_a \mathbf{N}_\eta$, $\mathbf{B}_b = \mathbf{L}_b \mathbf{N}_\eta$, $\overline{\mathbf{B}}_a = \overline{\mathbf{L}}_a \mathbf{N}_\eta$ and $\overline{\mathbf{B}}_b = \overline{\mathbf{L}}_b \mathbf{N}_\eta$. Note that $\mathbf{M}_\eta^e$ is not dependent on n while $\mathbf{V}_n^e$, $\mathbf{K}_n^e$ and $\mathbf{A}_n^e$ are functions of n, which means that they are evaluated for each n. Nevertheless, matrices $\mathbf{V}_n^e$ and $\mathbf{A}_n^e$ are expressed as polynomials with constant (matrix) coefficients multiplying a power of n and it is straightforward to express $\mathbf{K}_n^e$ in the same way. Finally, after assembling the element matrices into global matrices, the displacement harmonic amplitudes into $\boldsymbol{w}_n$ and the contact forces $\mathbf{F}_n$ of Eq. (49) into $\boldsymbol{\mathcal{F}}_n$, the EoM for each n greater than zero are given by:

$$\mathbf{M}_\eta \ddot{\boldsymbol{w}}_n(t) + 2\Omega \mathbf{V}_n \dot{\boldsymbol{w}}_n(t) + \left(\mathbf{K}_n + \Omega^2 \mathbf{A}_n\right) \boldsymbol{w}_n(t) = \boldsymbol{\mathcal{F}}_n(t). \tag{62}$$

If the model is transformed to the frequency domain, the EoM can be expressed for $\omega > 0$ as follows:

$$\left(-\omega^2 \mathbf{M}_\eta + 2\mathrm{i}\omega\Omega \mathbf{V}_n + \mathbf{K}_n + \Omega^2 \mathbf{A}_n\right) \boldsymbol{w}_n(\omega) = \boldsymbol{\mathcal{F}}_n(\omega). \tag{63}$$

4.5. Sound radiation

Considering the expression for the projected squared velocities in Eq. (29), the surface differentials $\mathrm{d}S_z$ and $\mathrm{d}S_r$ can be expressed as follows:

$$\begin{aligned} \mathrm{d}S_z &= r\mathrm{d}\theta\mathrm{d}r, \\ \mathrm{d}S_r &= r\mathrm{d}\theta\mathrm{d}z. \end{aligned} \tag{64}$$

The solution of the EoM for a given n results in the contribution of the set of vibration modes with n nodal diameters to the wheel response. Thus, for $n = 0$, considering the expressions of Eq. (30), the following relations are established:

$$\begin{aligned} v_{z,0}(r,z,\omega) &= \dot{w}_{z,0}(r,z,\omega) + \dot{\tau}_2(\omega), \\ v_{r,0}(r,z,\omega) &= \dot{w}_{r,0}(r,z,\omega), \end{aligned} \tag{65}$$

where the terms $\dot{w}_{z,0}$ and $\dot{w}_{r,0}$ are associated with the wheel flexibility and the term $\dot{\tau}_2$ with the wheelset RBM. Therefore, the integral in Eq. (29) can be evaluated analytically over the circumferential direction, yielding the following expressions:

$$\begin{aligned} S_z\langle\tilde{v}_{z,0}^2\rangle &= \pi \int_\Gamma |\dot{w}_{z,0} + \dot{\tau}_2|^2 r\mathrm{d}r, \\ S_r\langle\tilde{v}_{r,0}^2\rangle &= \pi \int_\Gamma |\dot{w}_{r,0}|^2 r\mathrm{d}z, \end{aligned} \tag{66}$$

where Γ is the wheel cross-section boundary. Similarly, for $n = 1$, according to Eq. (31), the following relations are satisfied:

$$\begin{aligned} v_{z,1}(r,\theta,z,\omega) &= \left(\dot{w}_{z,1}(r,z,\omega) - r\dot{\psi}_1(\omega)\right)\cos(\theta) - \left(\dot{\overline{w}}_{z,1}(r,z,\omega) - r\dot{\psi}_3(\omega)\right)\sin(\theta), \\ v_{r,1}(r,\theta,z,\omega) &= \left(\dot{w}_{r,1}(r,z,\omega) + \dot{\tau}_3(\omega) + z\dot{\psi}_1(\omega)\right)\cos(\theta) - \left(\dot{\overline{w}}_{r,1}(r,z,\omega) - \dot{\tau}_1(\omega) + z\dot{\psi}_3(\omega)\right)\sin(\theta), \end{aligned} \tag{67}$$

where the terms $\dot{w}_{z,1}$ and $\dot{w}_{r,1}$ are associated with the wheel flexibility and the rest with the wheelset RBM. Thus, the spatial average in Eq. (29) can be expressed as follows:

$$\begin{aligned} S_z\langle\tilde{v}_{z,1}^2\rangle &= \frac{\pi}{2}\int_\Gamma \left(|\dot{w}_{z,1} - r\dot{\psi}_1|^2 + |\dot{\overline{w}}_{z,1} - r\dot{\psi}_3|^2\right) r\mathrm{d}r, \\ S_r\langle\tilde{v}_{r,1}^2\rangle &= \frac{\pi}{2}\int_\Gamma \left(|\dot{w}_{r,1} + \dot{\tau}_3 + z\dot{\psi}_1|^2 + |\dot{\overline{w}}_{r,1} - \dot{\tau}_1 + z\dot{\psi}_3|^2\right) r\mathrm{d}z. \end{aligned} \tag{68}$$

Finally, for $n \geq 2$, the expression for the velocities in Eq. (32) can be written as:

$$v_{i,n}(r,\theta,z,\omega) = \dot{w}_{i,n}(r,z,\omega)\cos(n\theta) - \dot{\overline{w}}_{i,n}(r,z,\omega)\sin(n\theta), \quad i = z,r, \quad n \geq 2, \tag{69}$$

where the only contributions are from the wheel flexibility. The spatial average in Eq. (29) leads to the following expressions:

$$\begin{aligned} S_z\langle\tilde{v}_{z,n}^2\rangle &= \frac{\pi}{2}\int_\Gamma \left(|\dot{w}_{z,n}|^2 + |\dot{\overline{w}}_{z,n}|^2\right) r\mathrm{d}r, \quad n \geq 2, \\ S_r\langle\tilde{v}_{r,n}^2\rangle &= \frac{\pi}{2}\int_\Gamma \left(|\dot{w}_{r,n}|^2 + |\dot{\overline{w}}_{r,n}|^2\right) r\mathrm{d}z, \quad n \geq 2. \end{aligned} \tag{70}$$

Introducing Eqs. (66), (68) and (70) into Eq. (28), the sound radiation of a rotating wheel can be evaluated numerically in a two-dimensional frame.

5. Results

The model proposed in Section 4 is compared with the three-dimensional formulation presented in Section 3. Results are shown in terms of modal properties, frequency response functions (FRF), contact forces due to the wheel–rail interaction and sound power levels (SWL). For comparison, the FRF and SWL are also computed with the commercial package Ansys [18]; in this, the one-way FSI problem is solved (it is assumed that the air acoustic pressure does not to influence the wheel dynamics). Finally, the computational performance of the presented model, in terms of efficiency, is evaluated and benchmarked against the three-dimensional approach.

In this work, a railway wheel with straight web, a diameter of 900 mm and a mass of 345 kg is employed. Three-dimensional and cross-section two-dimensional FE meshes of this wheel are shown in Fig. 2, which are employed in the subsequent calculations. Quadratic elements are used in both approaches, considering 683 nodes in the two-dimensional FE discretization and 122628 nodes in the three-dimensional one, the latter having 132 elements around the circumferential direction. Note that, out of the 683 nodes in the 2D discretization, 246 are placed at the corners of the quadratic elements, so the number of nodes in the 3D FE model can be obtained as $132 \cdot (683 + 246) = 122628$. The wheel is constrained at the inner edge of the hub and, additionally, the wheelset RBM is superimposed on the response of the wheel according to the developments in Section 2. The wheelset has a mass of 1005 kg and moments of inertia of 88 kg m^2 and 580 kg m^2 about the axial and radial axes, respectively.

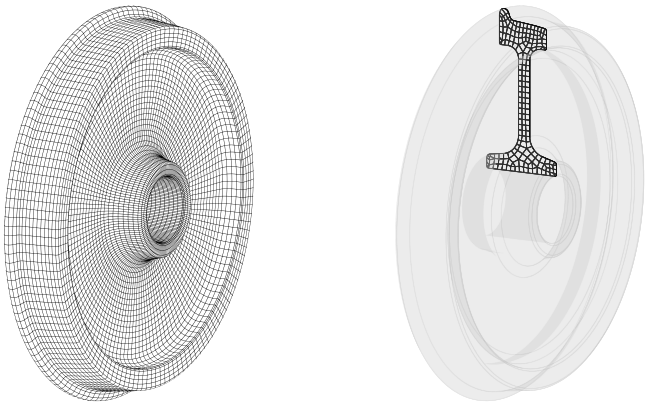

Fig. 2. Three-dimensional (left) and cross-section two-dimensional (right) FE meshes of the railway wheel.

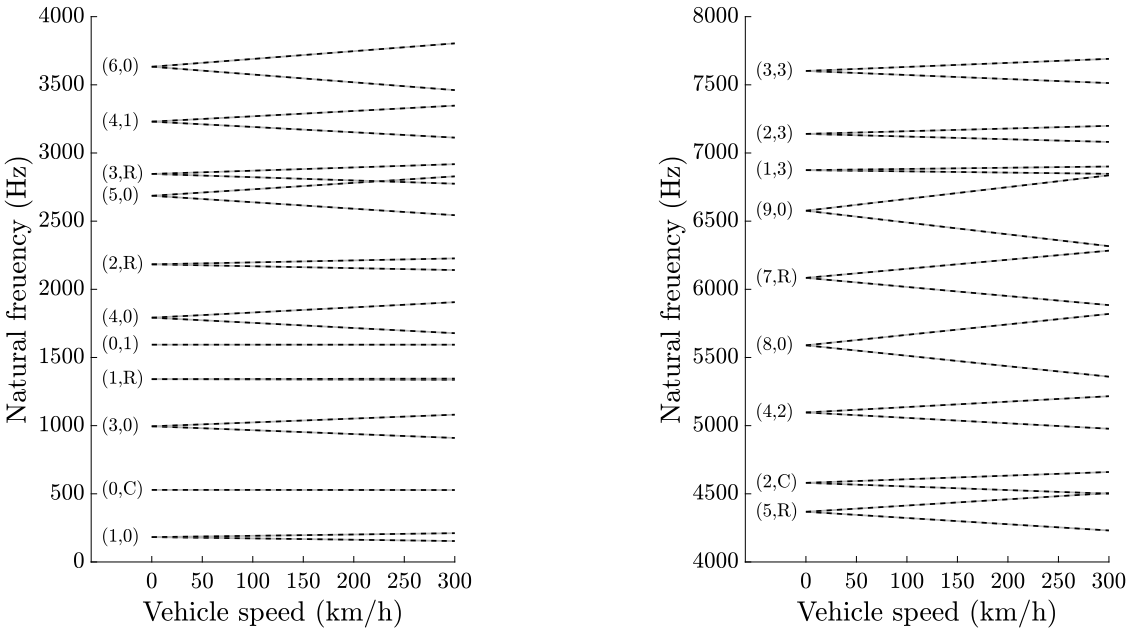

Fig. 3. Campbell diagram of the rotating wheel. Axial modeshapes are denoted as (n,m) while radial and circumferential modeshapes as (n,R) and (n,C), respectively. ——: Three-dimensional model; – – –: Axisymmetric approach.

5.1. Modal properties

Natural frequencies of the rotating wheel in the non-rotating frame are evaluated for different vehicle speeds. The results of the three-dimensional and axisymmetric models are presented for some modes in a Campbell diagram in Fig. 3. The maximum difference found between the two approaches is 0.44 Hz for a natural frequency of 6580 Hz, which represents a relative difference of 0.007%. Using the notation of Thompson [17], for the axial modes both the number of nodal diameters n and nodal circles m of each modeshape are given in the format (n,m) at the left of the lines. Regarding the radial and circumferential modes, since all the modeshapes presented in the Campbell diagram have $m = 0$, they are defined as (n,R) and (n,C), respectively.

5.2. Vibroacoustics

The wheel FRF at the contact point is evaluated through the three-dimensional and axisymmetric models for a vehicle speed of 80 km/h and the results are depicted in Fig. 4. As can be seen, there is no noticeable difference between the curves associated with the approaches presented in this work. A modal base formed by the vibration modes up to 12 kHz of the non-rotating wheel is considered for solving the EoM. Damping is included in the models using the empirical relation proposed by Thompson [17], in which the modal damping ratio ξ is related to the number of nodal diameters of the vibration mode, namely, $\xi = 10^{-3}$ for $n = 0$,

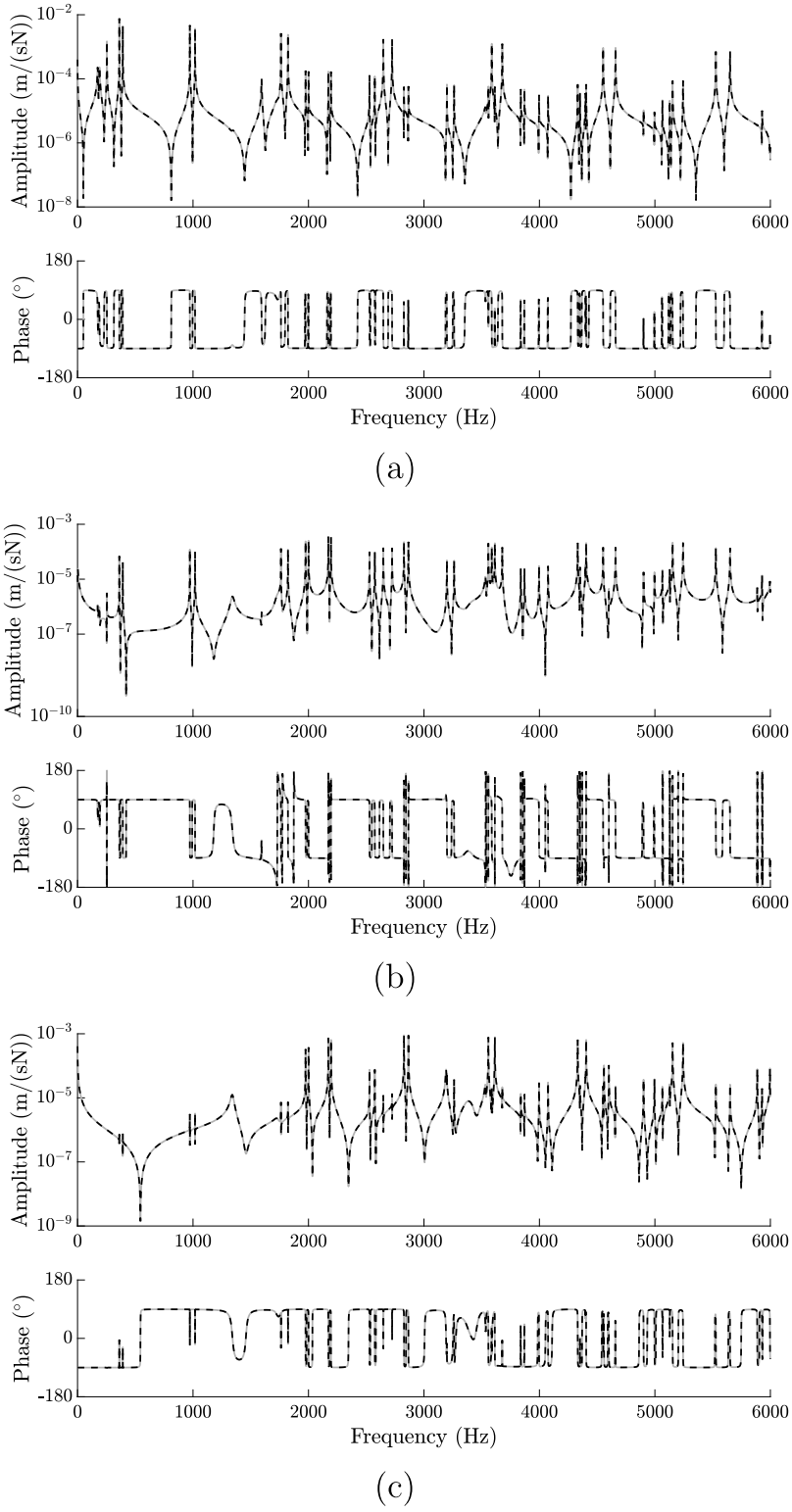

Fig. 4. Mobilities at the wheel contact point for a vehicle speed of 80 km/h. (a): direct axial/axial; (b): cross axial/radial; (c): direct radial/radial. ——: Three-dimensional model; – – –: Axisymmetric approach.

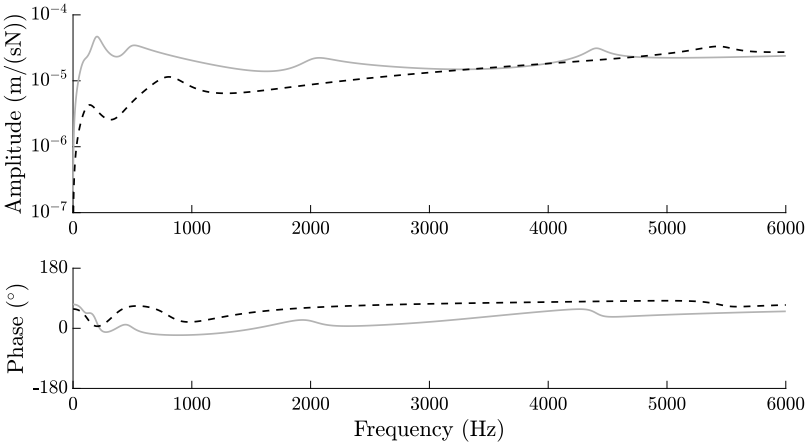

Fig. 5. Mobilities at the rail contact point. ——: direct lateral/lateral; – – –: direct vertical/vertical.

Table 1
Properties of the track model used in the wheel–rail interaction.

Rail pad stiffness[a] (MN/m^2)	1200 | 90
Rail pad damping loss factor (–)	0.375
Sleeper mass[b] (kg/m)	205
Ballast stiffness[a] (MN/m^2)	120 | 60
Ballast damping loss factor (–)	1.5

[a]Per unit length. Format: Vertical direction | Lateral direction.
[b]Per unit length. Corresponding to half sleeper.

$\xi = 10^{-2}$ for $n = 1$ and $\xi = 10^{-4}$ for $n \geq 2$. Also, the wheelset RBM contribution to the FRF is included in both methodologies. An adaptative frequency spacing is adopted based on the gradient of the contact receptances; the minimum resolution is 0.2 Hz and about 4000 different frequencies are evaluated.

The interaction forces due to the roughness present on the wheel and rail running surfaces are also evaluated for the radial and axial directions. In this work, the contact model proposed by Thompson [17,23] is used, in which the interaction forces are computed from the wheel and rail combined roughness by means of an operation involving the wheel and rail point receptances as well as the contact receptances. To do this, a continuous track model formed by a UIC60 rail profile supported by a spring–mass–spring system representing the rail pad, sleeper and ballast set is considered. The rail is modelled using periodic structure theory [24], the properties of the track are given in Table 1 and the FRF at the rail contact point are presented in Fig. 5; the cross lateral/vertical mobility is considered to be null. For the interaction problem, a vertical static load of 50 kN per wheel is considered, which has influence on the contact receptances. The wheel–rail interaction forces for a vehicle speed of 80 km/h and a unit roughness input at each frequency are presented in Fig. 6. As can be noted, both approaches predict practically the same forces at the contact.

Finally, the sound power radiated by the rotating wheel at a vehicle speed of 80 km/h is calculated. To do this, the roughness spectrum for cast iron brake blocks defined by the standard EN13979-1 [25] is introduced in the model through the procedure described by the aforementioned standard. Also, the contact filter proposed by Thompson [17] is included in the SWL computation. This is dependent on the vehicle velocity and the size of the contact area; in the contact model employed, the latter is a function of the vertical static load (50 kN) as well as the wheel and rail material properties and curvature radii in the contact points. The sound power levels, presented in one-third octave bands as A-weighted spectra [26], are shown in Fig. 7. Results without and with the wheelset RBM contribution to the wheel vibration are given. This contribution mainly increases the sound radiation below about 1 kHz, while in the high frequency range there is no significant influence. Considering the wheelset RBM, the maximum difference found in one-third octave band level between the three-dimensional and axisymmetric approaches is 0.05 dB(A). Note that the proposed methodology does not consider the flexible motion of the axle, which might influence the wheel SWL in the low and medium frequency range, where the acoustic energy radiated by the wheel is lower than in higher frequencies. Modelling this flexible motion could increase the complexity and computational effort of the models presented here and therefore it is not considered in this work.

For comparison purposes, the flexible wheel is also modelled in the commercial package Ansys [18]. This software implements the dynamic rotation model proposed by Geradin and Kill [10] for an inertial frame, in which a system of reference associated with local deformations is employed to describe the displacements and to formulate the equation of motion of a flexible rotating body. The rotation axis (axial direction) is the out-of-plane axis and the other two (longitudinal and vertical directions) are the in-plane axes. The local reference system is related to the inertial one by rotations about the two in-plane axes of the rotating body whereas

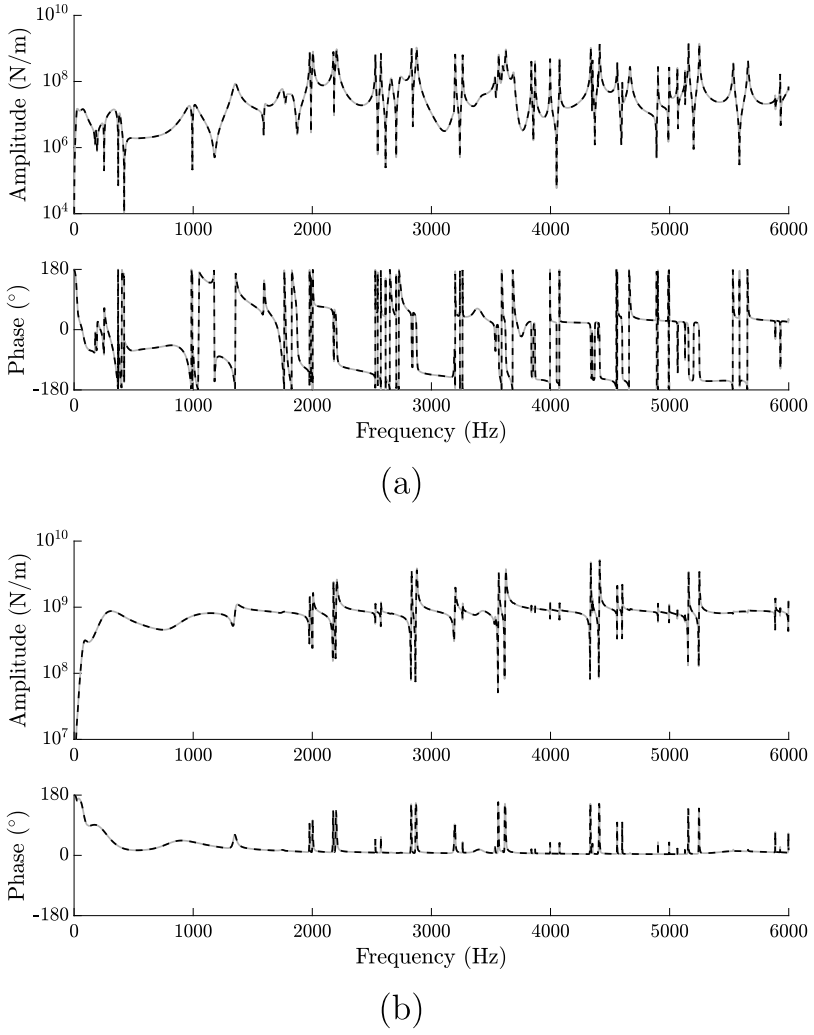

Fig. 6. Contact forces for a vehicle speed of 80 km/h and a unit roughness input. (a): axial; (b): radial. ——: Three-dimensional model; – – –: Axisymmetric approach.

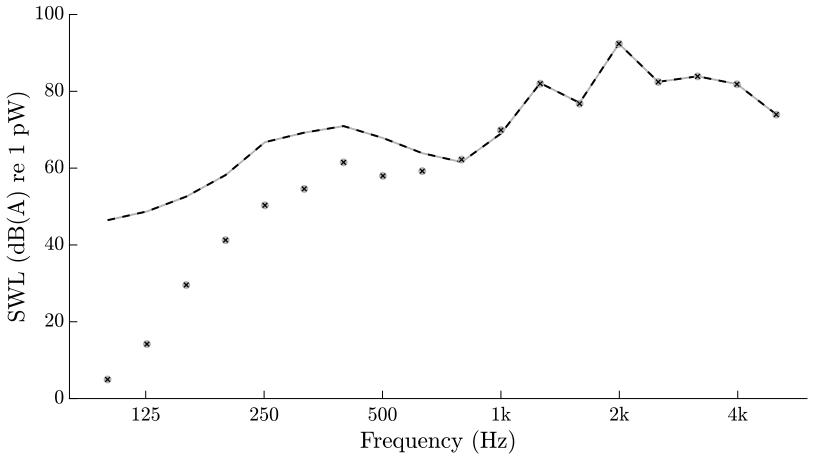

Fig. 7. SWL of the rotating wheel for a vehicle speed of 80 km/h. Lines include the wheelset RBM contribution while markers do not. —— and ●: Three-dimensional model; – – – and ×: Axisymmetric approach.

the rotation in the out-of-plane axis is only due to the rigid body spinning, so the torsional behaviour is not described by the model. The two rotations of the inertial system are assumed to be infinitesimal and so they are approximated by the first two terms of the Taylor expansion. This leads to the Eulerian and Lagrangian descriptions of in-plane coordinates being equivalent.

The 3D railway wheel is modelled in Ansys using the FEM (same mesh as in Fig. 2); then the rotation is included in the model and the receptances of the wheel at the contact point are evaluated for a given set of frequencies. These receptances are exported and used to solve the interaction forces through an in-house code. Subsequently, the computed forces are imported into Ansys and applied to the wheel contact point, allowing the wheel response to be calculated. Once the dynamics of the rotating wheel is solved, the wave equation for the surrounding air within a sphere of radius 1.55 m [18] is also modelled with the FEM considering the acoustic pressure as DoF; the FE model has 891317 nodes in the fluid region. The velocity on the wheel surface is prescribed as an acoustic boundary condition and, at the external surface of the fluid sphere, the Ansys *Radiation Boundary* condition is applied, which approximates the volume under consideration to infinity [18]. A comparison of the FRF and SWL delivered by this software with results from the vibroacoustic models proposed in this work is shown in Figs. 8 and 9, respectively. For this comparison, the wheelset RBM is not included in the models. Regarding the mobilities, the discrepancies are mainly found in the position of the two resonance peaks associated with natural frequencies of the wheel for $n > 0$, while the amplitudes are similar. In relation to the SWL, which is presented in one-third octave bands, there is a good agreement in most of the frequency range considered, the discrepancies being higher for lower frequencies. The main differences in the results between the proposed models and Ansys can be due to:

- The inclusion of the wheel rotation: Ansys implements the model developed by Geradin and Kill [10], briefly explained above.
- The methodology to solve the sound radiation: Ansys solves the one-way FSI problem whereas the proposed methodologies implement the acoustic model developed by Thompson [16]. This makes use of approximate expressions for radiation ratios, which are mostly influential in the low and medium frequency range, where the highest discrepancies are found in Fig. 9. Nevertheless, the energy contained in this frequency range is negligible compared with higher frequencies.

By adding the energy in each one-third octave frequency band, an overall SWL of 91.2 dB(A) is obtained by both the three-dimensional and axisymmetric approaches while 91.4 dB(A) is predicted by Ansys. It is also worth noting that the SWL given by the proposed models in Figs. 7 and 9 contain certain differences. The following reasons can be highlighted for this:

- As mentioned above, for simplicity, the wheelset RBM contribution to the flexible wheel motion is not included in the comparison with Ansys (Fig. 9), which introduces some differences in the low frequency range (see Fig. 7).
- Given the high computational cost associated with the acoustic calculation in Ansys, about 2250 different frequencies are evaluated in producing Fig. 9 with a minimum resolution of 1 Hz. As explained at the beginning of this Section, about 4000 frequencies with a minimum resolution of 0.2 Hz are considered in Fig. 7.
- When including rotation in Ansys, it is not possible to solve the wheel dynamics using a modal approach and the direct method is employed by inverting the EoM formulated in physical coordinates. Thus, the modal damping defined at the beginning of this Section, and considered in Fig. 7, cannot be included in the model in Ansys. Instead, a proportional damping with a mass multiplier of 19.9 and a stiffness multiplier of $1.24 \cdot 10^{-8}$ is considered to compute the three curves in Fig. 9. The matrix multipliers have been tuned to produce modal damping values as similar as possible to those used in Fig. 7.
- As stated in the previous paragraph, the solution of the EoM in Ansys is performed by the direct method. In the proposed methodologies, a modal approach is adopted, considering as modal basis the vibration modes with natural frequencies below 12 kHz. The difference between the proposed methodologies and Ansys corresponds to the contribution of higher order modes, which can be assumed constant in the frequency range studied (up to 6 kHz) [27]. Therefore, this contribution can be evaluated as the difference between the direct static solution (inversion of the stiffness matrix) and the solution for zero frequency using the modal approach. In Fig. 9, in order to minimize the differences with Ansys, the aforementioned contribution is added to the dynamic solution of the modal approach, but it has not been included in Fig. 7.

The previous four reasons also explain the differences between Figs. 4 and 8 regarding the results given by the proposed models. It is worth noting that the methodology proposed in this work, which leads to Figs. 4 and 7, is the more physically correct.

5.3. Computational performance

The methodology used in the axisymmetric approach presented consists of solving the circumferential direction analytically and the other two dimensions numerically. This procedure, as opposed to the full three-dimensional methodology, suppresses the discretization error associated with the FEM in the circumferential direction. When using FE meshes with a sufficiently large number of nodes, the results obtained from the two models are indistinguishable. Nevertheless, the performance of the axisymmetric approach model is far superior in terms of computational effort.

To evaluate the computational performance, the SWL results from different FE meshes are compared with those from a highly refined three-dimensional FE mesh with 358592 nodes, which is consider as the reference case. Both the computational time required for the calculation of each FE mesh and the discrepancy with respect to the reference case are determined. The discrepancy for the ith FE mesh is defined as the average of the absolute difference in decibels for each one-third octave frequency band between the SWL for the ith case and the reference one. The same frequency resolution technique as explained in Section 5.2 is used in this analysis. In Fig. 10(a) the relation between the discrepancy and computational calculation time from both models is shown

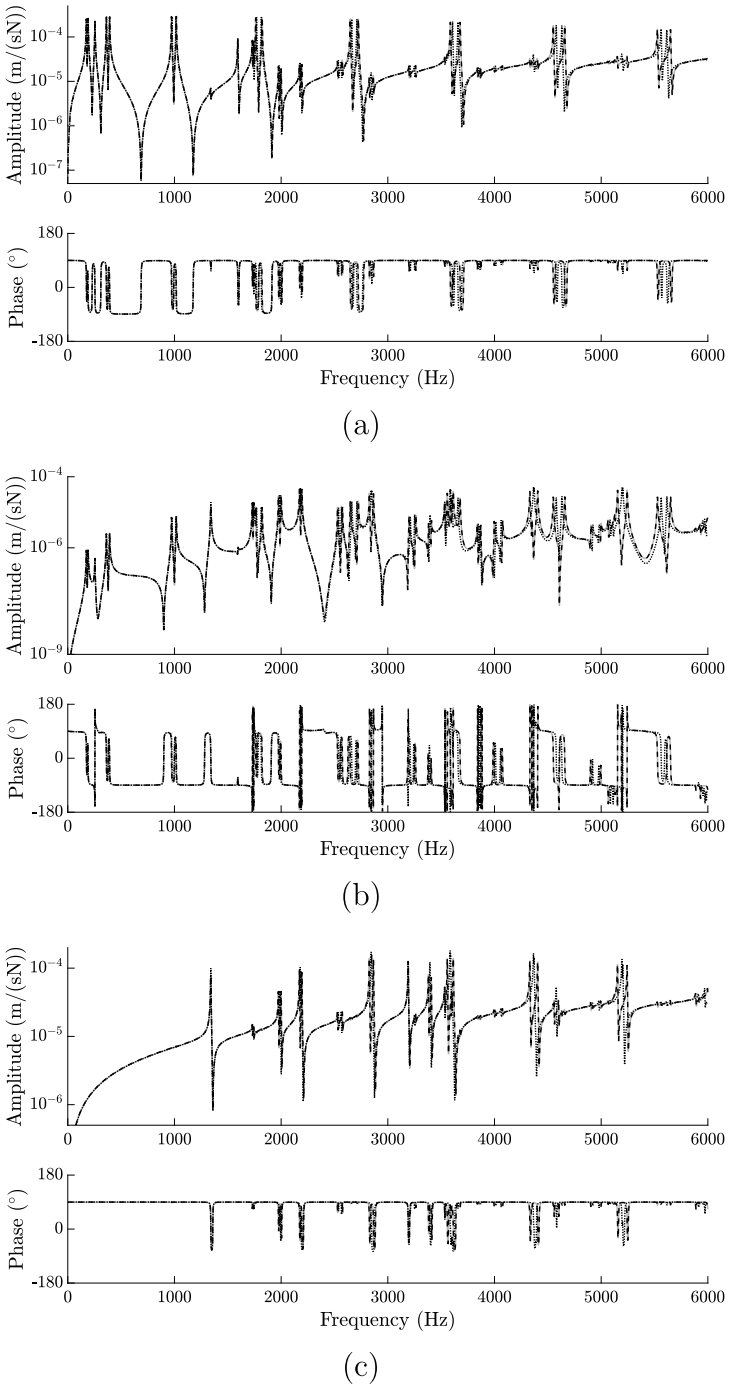

Fig. 8. Comparison of the mobilities at the wheel contact point for a vehicle speed of 80 km/h. (a): direct axial/axial; (b): cross axial/radial; (c): direct radial/radial. ——: Three-dimensional model; – – –: Axisymmetric approach; ·····: Ansys.

for each FE mesh (circle markers) and, in particular, for the meshes employed in the previous results (cross markers). Also, a regression line which fits the results is proposed. This allows the ratio to be evaluated between the computational time of the three-dimensional and axisymmetric approaches for a given discrepancy, which is shown in Fig. 10(b). The axisymmetric approach is, for small discrepancies, approximately three orders of magnitude more efficient than the three-dimensional one, which makes the former suitable for implementation in optimization algorithms or SWL minimization routines. The numerical simulations are carried out in a PC running with an®Intel i7-9700 processor with 64 GB RAM. Regarding the calculations performed in Ansys, for

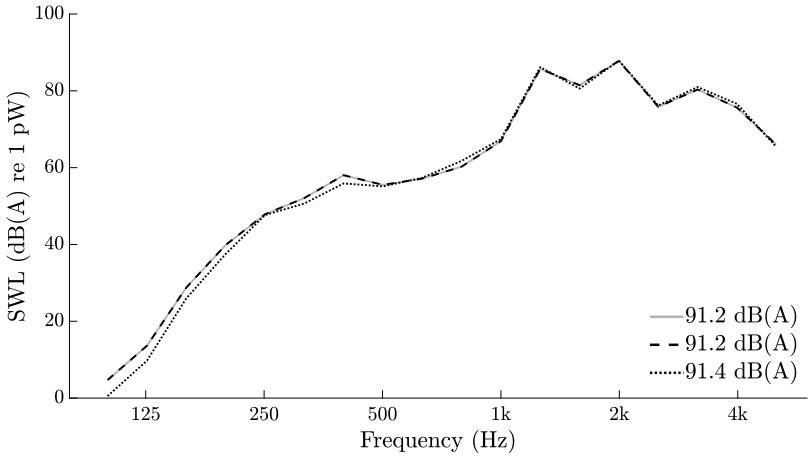

Fig. 9. SWL comparison of the rotating wheel for a vehicle speed of 80 km/h. ——: Three-dimensional model; – – –: Axisymmetric approach; ·····: Ansys.

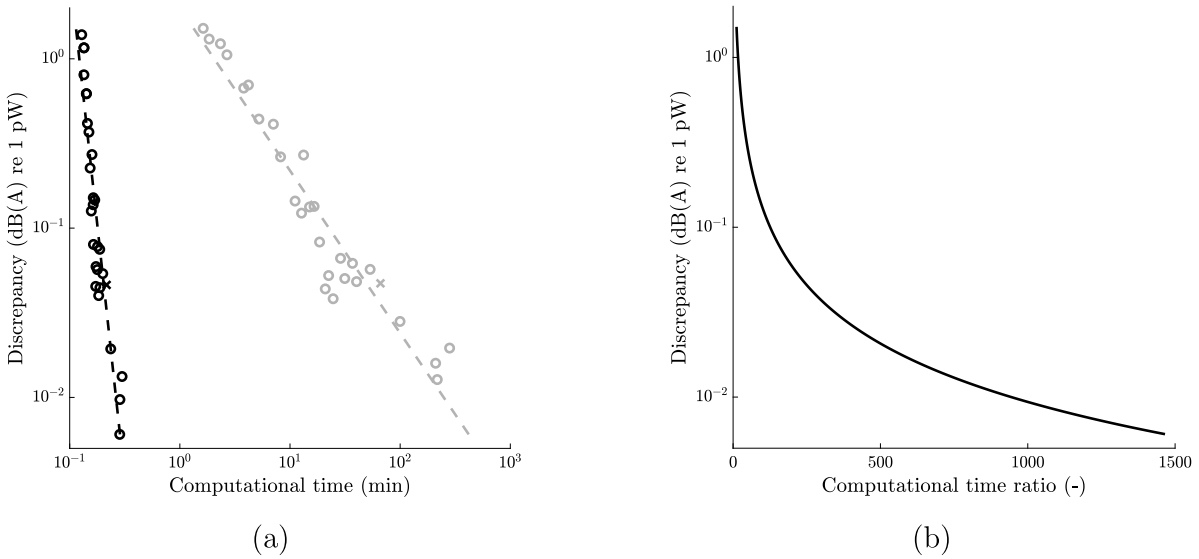

Fig. 10. (a): Discrepancy in the SWL results for the different FE meshes (markers), including the two used in the previous results (cross markers), and regression (dashed lines) for the three-dimensional (grey) and axisymmetric (black) models; (b): Discrepancy as a function of the ratio between the computational time from the three-dimensional and axisymmetric models.

2250 different frequencies a total time of approximately 11.5 days is required, which represents a computational cost five orders of magnitude higher than that of the axisymmetric approach .

6. Conclusions

A model of an axisymmetric rotating and flexible railway wheel is proposed which allows a solution in a two-dimensional frame for both the dynamic response and the sound radiation of the wheel due to its interaction with the rail. The wheelset RBM is described through an analytical model and it is superimposed on the wheel vibration, which is constrained at the inner edge of the hub. The proposed models are specifically aimed at describing the vibroacoustic behaviour of a railway wheel, but in general they are valid for any rotating system provided that axisymmetry exists.

First, a three-dimensional vibroacoustic model of the rotating flexible wheel, numerically addressed through the FEM, is presented. The response of the wheel around the circumferential direction is then expanded using Fourier series, which allows the dynamic and acoustic fields to be solved analytically in that direction. The other two directions, associated with the wheel cross-section, are solved numerically. Finally, the rigid wheelset motion, which is solved analytically, is superimposed on the flexible wheel motion; this mainly modifies the wheel response in the low frequency range. Further development of this model could consider the flexible motion of the axle which is subject for future study.

The results from the proposed axisymmetric model are compared with the three-dimensional methodology in terms of modal, dynamic and acoustic behaviour, obtaining virtually identical solutions. In addition, the SWL predicted from both aforementioned methodologies are compared with those from the commercial package Ansys and similar results are obtained although some discrepancies, mainly in the low frequency range, are noted. However, in overall terms, a difference of only 0.2 dB(A) is found.

The axisymmetric approach presented suppresses the discretization error associated with the FEM in the circumferential direction, therefore leading to similar results to the three-dimensional model when considering highly refined FE meshes. However, for these meshes, the computational time required by the proposed axisymmetric model to solve the sound radiation of the wheel is approximately 1000 times less than with the three-dimensional methodology.

CRediT authorship contribution statement

V.T. Andrés: Conceptualization, Methodology, Software, Validation, Writing – original draft. **J. Martínez-Casas:** Conceptualization, Methodology, Writing – review & editing, Supervision, Project administration, Funding acquisition. **F.D. Denia:** Conceptualization, Methodology, Writing – review & editing, Supervision, Project administration, Funding acquisition. **D.J. Thompson:** Conceptualization, Methodology, Writing – review & editing, Supervision.

Declaration of competing interest

The authors declare that they have no known competing financial interests or personal relationships that could have appeared to influence the work reported in this paper.

Data availability

Data will be made available on request.

Acknowledgements

This paper is part of the project PID2020-112886RA-I00, grant FPU18/03999 and grant EST21/00213 funded by MCIN/AEI/10.13039/501100011033 as well as by "ESF Investing in your future". The authors also acknowledge Programa PROMETEO/2021/046 of Generalitat Valenciana, Spain.

Appendix A. Matrices and matrix operators

A.1. Matrices

$$\mathbf{K}_1 = \begin{bmatrix} 0 & 0 & -1 \\ 0 & 0 & 0 \\ 1 & 0 & 0 \end{bmatrix}, \qquad \mathbf{K}_2 = \begin{bmatrix} \frac{1}{2} & 0 & 0 \\ 0 & 1 & 0 \\ 0 & 0 & \frac{1}{2} \end{bmatrix}. \tag{A.1}$$

$$\mathbf{J} = \begin{bmatrix} 0 & -1 & 0 \\ 1 & 0 & 0 \\ 0 & 0 & 0 \end{bmatrix}, \qquad \mathbf{E} = \mathbf{J}^{\mathrm{T}}\mathbf{J} = \begin{bmatrix} 1 & 0 & 0 \\ 0 & 1 & 0 \\ 0 & 0 & 0 \end{bmatrix}. \tag{A.2}$$

$$\mathbf{D} = \frac{\lambda}{(1+\nu)(1-2\nu)} \begin{bmatrix} 1-\nu & \nu & \nu & 0 & 0 & 0 \\ \nu & 1-\nu & \nu & 0 & 0 & 0 \\ \nu & \nu & 1-\nu & 0 & 0 & 0 \\ 0 & 0 & 0 & \frac{1-2\nu}{2} & 0 & 0 \\ 0 & 0 & 0 & 0 & \frac{1-2\nu}{2} & 0 \\ 0 & 0 & 0 & 0 & 0 & \frac{1-2\nu}{2} \end{bmatrix}, \tag{A.3}$$

with λ being the Young's modulus and ν the Poisson's ratio.

$$\mathbf{J}_0 = \begin{bmatrix} 0 & 0 & 1 \\ 0 & 0 & 0 \\ -1 & 0 & 0 \end{bmatrix}, \qquad \mathbf{E}_0 = \mathbf{J}_0^{\mathrm{T}}\mathbf{J}_0 = \begin{bmatrix} 1 & 0 & 0 \\ 0 & 0 & 0 \\ 0 & 0 & 1 \end{bmatrix}. \tag{A.4}$$

$$\mathbf{J}_1 = \begin{bmatrix} 0 & 1 & 0 & 0 & 0 & 0 \\ 0 & 0 & 0 & 0 & 0 & 0 \\ 0 & 0 & 0 & 0 & 0 & 0 \\ 0 & 0 & 0 & 0 & -1 & 0 \\ 0 & 0 & 0 & 0 & 0 & 0 \\ 0 & 0 & 0 & 0 & 0 & 0 \end{bmatrix}, \quad \mathbf{J}_2 = \begin{bmatrix} 0 & 0 & 0 & -1 & 0 & 0 \\ 0 & 0 & 0 & 0 & 1 & 0 \\ 0 & 0 & 0 & 0 & 0 & -1 \\ 1 & 0 & 0 & 0 & 0 & 0 \\ 0 & -1 & 0 & 0 & 0 & 0 \\ 0 & 0 & 1 & 0 & 0 & 0 \end{bmatrix},$$
$$\mathbf{J}_3 = \begin{bmatrix} 0 & 0 & 0 & 0 & 1 & 0 \\ 0 & 0 & 0 & -1 & 0 & 0 \\ 0 & 0 & 0 & 0 & 0 & 0 \\ 0 & 1 & 0 & 0 & 0 & 0 \\ -1 & 0 & 0 & 0 & 0 & 0 \\ 0 & 0 & 0 & 0 & 0 & 0 \end{bmatrix}, \quad \mathbf{E}_3 = \mathbf{J}_3^{\mathrm{T}}\mathbf{J}_3 = \begin{bmatrix} 1 & 0 & 0 & 0 & 0 & 0 \\ 0 & 1 & 0 & 0 & 0 & 0 \\ 0 & 0 & 0 & 0 & 0 & 0 \\ 0 & 0 & 0 & 1 & 0 & 0 \\ 0 & 0 & 0 & 0 & 1 & 0 \\ 0 & 0 & 0 & 0 & 0 & 0 \end{bmatrix}. \tag{A.5}$$

A.2. Matrix operators

$$\mathbf{L} = \begin{bmatrix} \frac{\partial}{\partial r} & 0 & 0 \\ \frac{1}{r} & \frac{1}{r}\frac{\partial}{\partial \theta} & 0 \\ 0 & 0 & \frac{\partial}{\partial z} \\ \frac{\partial}{\partial z} & 0 & \frac{\partial}{\partial r} \\ \frac{1}{r}\frac{\partial}{\partial \theta} & \frac{\partial}{\partial r} - \frac{1}{r} & 0 \\ 0 & \frac{\partial}{\partial z} & \frac{1}{r}\frac{\partial}{\partial \theta} \end{bmatrix}. \tag{A.6}$$

$$\mathbf{L}_0 = \begin{bmatrix} \frac{\partial}{\partial r} & 0 & 0 \\ \frac{1}{r} & 0 & 0 \\ 0 & \frac{\partial}{\partial z} & 0 \\ \frac{\partial}{\partial z} & \frac{\partial}{\partial r} & 0 \\ 0 & 0 & \frac{\partial}{\partial r} - \frac{1}{r} \\ 0 & 0 & \frac{\partial}{\partial z} \end{bmatrix}. \tag{A.7}$$

$$\mathbf{L}_a = \begin{bmatrix} \frac{\partial}{\partial r} & 0 & 0 & 0 & 0 & 0 \\ \frac{1}{r} & 0 & 0 & 0 & 0 & 0 \\ 0 & 0 & \frac{\partial}{\partial z} & 0 & 0 & 0 \\ \frac{\partial}{\partial z} & 0 & \frac{\partial}{\partial r} & 0 & 0 & 0 \\ 0 & \frac{\partial}{\partial r} - \frac{1}{r} & 0 & 0 & 0 & 0 \\ 0 & \frac{\partial}{\partial z} & 0 & 0 & 0 & 0 \end{bmatrix}, \quad \mathbf{L}_b = \begin{bmatrix} 0 & 0 & 0 & 0 & 0 & 0 \\ 0 & \frac{1}{r} & 0 & 0 & 0 & 0 \\ 0 & 0 & 0 & 0 & 0 & 0 \\ 0 & 0 & 0 & 0 & 0 & 0 \\ -\frac{1}{r} & 0 & 0 & 0 & 0 & 0 \\ 0 & 0 & -\frac{1}{r} & 0 & 0 & 0 \end{bmatrix},$$
$$\overline{\mathbf{L}}_a = \begin{bmatrix} 0 & 0 & 0 & \frac{\partial}{\partial r} & 0 & 0 \\ 0 & 0 & 0 & \frac{1}{r} & 0 & 0 \\ 0 & 0 & 0 & 0 & 0 & \frac{\partial}{\partial z} \\ 0 & 0 & 0 & \frac{\partial}{\partial z} & 0 & \frac{\partial}{\partial r} \\ 0 & 0 & 0 & 0 & \frac{\partial}{\partial r} - \frac{1}{r} & 0 \\ 0 & 0 & 0 & 0 & \frac{\partial}{\partial z} & 0 \end{bmatrix}, \quad \overline{\mathbf{L}}_b = \begin{bmatrix} 0 & 0 & 0 & 0 & 0 & 0 \\ 0 & 0 & 0 & 0 & -\frac{1}{r} & 0 \\ 0 & 0 & 0 & 0 & 0 & 0 \\ 0 & 0 & 0 & 0 & 0 & 0 \\ 0 & 0 & 0 & \frac{1}{r} & 0 & 0 \\ 0 & 0 & 0 & 0 & 0 & \frac{1}{r} \end{bmatrix}. \tag{A.8}$$

Appendix B. Kinetic and strain energy integration

In this appendix the analytical integration in the circumferential direction of the kinetic energy in Eq. (18) and strain energy in Eq. (19) is detailed. To compute the integrals, considering $n, l \in \mathbb{Z}$, the following relations are used:

$$\begin{aligned}
&\int_{-\pi}^{\pi} \sin(n\theta)\sin(l\theta)\mathrm{d}\theta = \begin{cases} \pi, & \text{if} \quad n = l \neq 0. \\ 0, & \text{if} \quad n \neq l \ \text{ or } \ n = l = 0. \end{cases} \\
&\int_{-\pi}^{\pi} \cos(n\theta)\cos(l\theta)\mathrm{d}\theta = \begin{cases} \pi, & \text{if} \quad n = l \neq 0. \\ 0, & \text{if} \quad n \neq l. \\ 2\pi, & \text{if} \quad n = l = 0. \end{cases} \\
&\int_{-\pi}^{\pi} \sin(n\theta)\cos(l\theta)\mathrm{d}\theta = 0, \quad \forall n, l.
\end{aligned} \tag{B.1}$$

Bearing in mind that $\mathrm{d}V = r\mathrm{d}\theta\mathrm{d}A$ and decomposing the kinetic energy into its ten terms, the result of the aforementioned integration is given by:

$$E_k^{(1)} = \frac{1}{2}\Omega^2 \int_V \rho r^2 \mathrm{d}V = \pi\Omega^2 \int_A \rho r^3 \mathrm{d}A, \tag{B.2a}$$

$$E_k^{(2)} = \frac{1}{2}\int_V \rho \dot{\mathbf{w}}^{\mathrm{T}}\dot{\mathbf{w}}\mathrm{d}V = \pi \int_A \rho r \dot{\mathbf{w}}_0^{\mathrm{T}}\dot{\mathbf{w}}_0 \mathrm{d}A + \sum_{n>0}\left(\frac{\pi}{2}\int_A \rho r \dot{\mathbf{w}}_n^{\mathrm{T}}\dot{\mathbf{w}}_n \mathrm{d}A\right), \tag{B.2b}$$

$$E_k^{(3)} = \frac{1}{2}\Omega^2 \int_V \rho \frac{\partial \mathbf{w}^{\mathrm{T}}}{\partial\theta}\frac{\partial \mathbf{w}}{\partial\theta}\mathrm{d}V = \sum_{n>0}\left(\frac{\pi}{2}\Omega^2 \int_A \rho r n^2 \mathbf{w}_n^{\mathrm{T}}\mathbf{w}_n \mathrm{d}A\right), \tag{B.2c}$$

$$E_k^{(4)} = \Omega^2 \int_V \rho \frac{\partial \mathbf{w}^{\mathrm{T}}}{\partial\theta}\mathbf{J}\mathbf{w}\mathrm{d}V = \sum_{n>0}\left(2\pi\Omega^2 \int_A \rho r n \mathbf{w}_n^{\mathrm{T}}\mathbf{J}_1\mathbf{w}_n \mathrm{d}A\right), \tag{B.2d}$$

$$E_k^{(5)} = \Omega \int_V \rho r \hat{\mathbf{e}}_2^{\mathrm{T}}\dot{\mathbf{w}}\mathrm{d}V = -2\pi\Omega \int_A \rho r^2 \hat{\mathbf{e}}_3^{\mathrm{T}}\dot{\mathbf{w}}_0 \mathrm{d}A, \tag{B.2e}$$

$$E_k^{(6)} = \Omega^2 \int_V \rho r \hat{\mathbf{e}}_2^{\mathrm{T}}\frac{\partial \mathbf{w}}{\partial\theta}\mathrm{d}V = 0, \tag{B.2f}$$

$$E_k^{(7)} = \Omega^2 \int_V \rho r \hat{\mathbf{e}}_2^{\mathrm{T}}\mathbf{J}\mathbf{w}\mathrm{d}V = 2\pi\Omega^2 \int_A \rho r^2 \hat{\mathbf{e}}_1^{\mathrm{T}}\mathbf{w}_0 \mathrm{d}A, \tag{B.2g}$$

$$E_k^{(8)} = \Omega \int_V \rho \dot{\mathbf{w}}^{\mathrm{T}}\frac{\partial \mathbf{w}}{\partial\theta}\mathrm{d}V = \sum_{n>0}\left(\pi\Omega \int_A \rho r n \dot{\mathbf{w}}_n^{\mathrm{T}}\mathbf{J}_2\mathbf{w}_n \mathrm{d}A\right), \tag{B.2h}$$

$$E_k^{(9)} = \Omega \int_V \rho \dot{\mathbf{w}}^{\mathrm{T}}\mathbf{J}\mathbf{w}\mathrm{d}V = 2\pi\Omega \int_A \rho r \dot{\mathbf{w}}_0^{\mathrm{T}}\mathbf{J}_0\mathbf{w}_0 \mathrm{d}A + \sum_{n>0}\left(\pi\Omega \int_A \rho r \dot{\mathbf{w}}_n^{\mathrm{T}}\mathbf{J}_3\mathbf{w}_n \mathrm{d}A\right), \tag{B.2i}$$

$$E_k^{(10)} = \frac{1}{2}\Omega^2 \int_V \rho \mathbf{w}^{\mathrm{T}}\mathbf{E}\mathbf{w}\mathrm{d}V = \pi\Omega^2 \int_A \rho r \mathbf{w}_0^{\mathrm{T}}\mathbf{E}_0\mathbf{w}_0 \mathrm{d}A + \sum_{n>0}\left(\frac{\pi}{2}\Omega^2 \int_A \rho r \mathbf{w}_n^{\mathrm{T}}\mathbf{E}_3\mathbf{w}_n \mathrm{d}A\right). \tag{B.2j}$$

Similarly, considering the strain energy, the following expression is computed:

$$E_p = \frac{1}{2}\int_V \boldsymbol{\varepsilon}^{\mathrm{T}}\mathbf{D}\boldsymbol{\varepsilon}\mathrm{d}V = \pi \int_A r\boldsymbol{\varepsilon}_0^{\mathrm{T}}\mathbf{D}\boldsymbol{\varepsilon}_0 \mathrm{d}A + \sum_{n>0}\left(\frac{\pi}{2}\int_A r\boldsymbol{\varepsilon}_n^{\mathrm{T}}\mathbf{D}\boldsymbol{\varepsilon}_n \mathrm{d}A + \frac{\pi}{2}\int_A r\bar{\boldsymbol{\varepsilon}}_n^{\mathrm{T}}\mathbf{D}\bar{\boldsymbol{\varepsilon}}_n \mathrm{d}A\right). \tag{B.3}$$

References

[1] C.J.C. Jones, D.J. Thompson, Rolling noise generated by railway wheels with visco-elastic layers, J. Sound Vib. 231 (3) (2000) 779–790, http://dx.doi.org/10.1006/jsvi.1999.2562.

[2] F. Létourneaux, J.F. Cordier, F. Poisson, N. Douarche, High speed railway noise: assessment of mitigation measures, in: B. Schulte-Werning, et al. (Eds.), Proceedings of 9th International Workshop on Railway Noise, Munich, Germany, 4–8 September 2007, in: Notes on Numerical Fluid Mechanics & Multidisciplinary Design, 99, 2008, pp. 56–62, http://dx.doi.org/10.1007/978-3-540-74893-9_8.

[3] D.J. Thompson, C.J.C. Jones, T.P. Waters, D. Farrington, A tuned damping device for reducing noise from railway track, Appl. Acoust. 68 (1) (2007) 43–57, http://dx.doi.org/10.1016/j.apacoust.2006.05.001.

[4] J.C.O. Nielsen, C.R. Fredö, Multi-disciplinary optimization of railway wheels, J. Sound Vib. 293 (3) (2006) 510–521, http://dx.doi.org/10.1016/j.jsv.2005.08.063.

[5] X. Garcia-Andrés, J. Gutiérrez-Gil, J. Martínez-Casas, F.D. Denia, Wheel shape optimization approaches to reduce railway rolling noise, Struct. Multidiscip. Optim. 62 (2020) 2555–2570, http://dx.doi.org/10.1007/s00158-020-02700-6.

[6] J. Gutiérrez-Gil, X. Garcia-Andrés, J. Martínez-Casas, E. Nadal, F.D. Denia, Optimized perforation schemes in railway wheels toward acoustic radiation mitigation, J. Vib. Acoust. 142 (4) (2020) 041009, http://dx.doi.org/10.1115/1.4046681.

[7] V.T. Andrés, J. Martínez-Casas, F.D. Denia, D.J. Thompson, Influence study of rail geometry and track properties on railway rolling noise, J. Sound Vib. 525 (2022) 116701, http://dx.doi.org/10.1016/j.jsv.2021.116701.

[8] D.J. Thompson, Wheel-rail noise generation, part II: Wheel vibration, J. Sound Vib. 161 (3) (1993) 401–419, http://dx.doi.org/10.1006/jsvi.1993.1083.

[9] D.J. Thompson, Wheel-rail noise generation, part V: Inclusion of wheel rotation, J. Sound Vib. 161 (3) (1993) 467–482, http://dx.doi.org/10.1006/jsvi.1993.1086.

[10] M. Geradin, N. Kill, A new approach to finite element modelling of flexible rotors, Eng. Comput. 1 (1) (1984) 52–64, http://dx.doi.org/10.1108/eb023560.

[11] G. Genta, A. Tonoli, A harmonic finite element for the analysis of flexural, torsional and axial rotordynamic behaviour of discs, J. Sound Vib. 196 (1) (1996) 19–43, http://dx.doi.org/10.1006/jsvi.1996.0465.
[12] X. Sheng, Y. Liu, X. Zhou, The response of a high-speed train wheel to a harmonic wheel–rail force, J. Phys. Conf. Ser. 744 (2016) 012145, http://dx.doi.org/10.1088/1742-6596/744/1/012145.
[13] J. Fayos, L. Baeza, F.D. Denia, J.E. Tarancón, An Eulerian coordinate-based method for analysing the structural vibrations of a solid of revolution rotating about its main axis, J. Sound Vib. 306 (3) (2007) 618–635, http://dx.doi.org/10.1016/j.jsv.2007.05.051.
[14] J. Martínez-Casas, L. Mazzola, L. Baeza, S. Bruni, Numerical estimation of stresses in railway axles using a train–track interaction model, Int. J. Fatigue 47 (2013) 18–30, http://dx.doi.org/10.1016/j.ijfatigue.2012.07.006.
[15] L. Baeza, J. Giner-Navarro, D.J. Thompson, J. Monterde, Eulerian models of the rotating flexible wheelset for high frequency railway dynamics, J. Sound Vib. 449 (2019) 300–314, http://dx.doi.org/10.1016/j.jsv.2019.03.002.
[16] D.J. Thompson, C.J.C. Jones, Sound radiation from a vibrating railway wheel, J. Sound Vib. 253 (2) (2002) 401–419, http://dx.doi.org/10.1006/jsvi.2001.4061.
[17] D.J. Thompson, Railway noise and vibration. Mechanisms, modelling and means of control, Elsevier, ISBN: 978-0-08-045147-3, 2009, http://dx.doi.org/10.1016/B978-0-08-045147-3.X0023-0.
[18] Ansys® Academic Research Mechanical, Release 19.2, Help System, ANSYS, Inc.
[19] G.K. Batchelor, An introduction to fluid dynamics, Cambridge University Press, ISBN: 9780511800955, 2000, http://dx.doi.org/10.1017/CBO9780511800955.
[20] R.B. Bird, W.E. Stewart, E.N. Lightfoot, Transport Phenomena, Revised, second ed., John Wiley & Sons, ISBN: 978-0-470-11539-8, 2006.
[21] O.C. Zienkiewicz, R.L. Taylor, J.Z. Zhu, The Finite Element Method: Its Basis and Fundamentals, seventh ed., Butterworth-Heinemann, ISBN: 978-1-85617-633-0, 2013, http://dx.doi.org/10.1016/C2009-0-24909-9.
[22] M. Petyt, Introduction to finite element vibration analysis, second ed., Cambridge University Press, ISBN: 9780521191609, 2010, http://dx.doi.org/10.1017/CBO9780511761195.
[23] D.J. Thompson, Wheel-rail noise generation, part I: Introduction and interaction model, J. Sound Vib. 161 (3) (1993) 387–400, http://dx.doi.org/10.1006/jsvi.1993.1082.
[24] D.J. Thompson, Wheel-rail noise generation, part III: Rail vibration, J. Sound Vib. 161 (3) (1993) 421–446, http://dx.doi.org/10.1006/jsvi.1993.1084.
[25] Railway applications – Wheelsets and bogies – Monobloc wheels – Technical approval procedure – Part 1: Forged and rolled wheels, EN 13979-1:2020, European Committee for Standardization, 2020.
[26] Electroacoustics – Sound level meters – Part 1: Specifications, IEC 61672-1:2013, International Electrotechnical Commission, 2013.
[27] O.E. Hansteen, K. Bell, On the accuracy of mode superposition analysis in structural dynamics, Earthq. Eng. Struct. Dyn. 7 (5) (1979) 405–411, http://dx.doi.org/10.1002/eqe.4290070502.